

Pasta structures in compact stars

Toshiki Maruyama

Advanced Science Research Center, Japan Atomic Energy Agency, Tokai, Ibaraki,
319-1195 Japan

Toshitaka Tatsumi

Department of Physics, Kyoto University, Kyoto 606-8502, Japan

Tomoki Endo¹

Department of Physics, Kyoto University, Kyoto 606-8502, Japan

Satoshi Chiba

Advanced Science Research Center, Japan Atomic Energy Agency, Tokai, Ibaraki,
319-1195 Japan

We review our recent works about “pasta” structures following the first-order phase transition in dense matter, which correspond to the structured mixed phases with geometrical symmetries. Three kinds of phase transitions at different density ranges are examined as the stages of pasta structures: liquid-gas phase transition at subnuclear density, kaon condensation and hadron-quark phase transition at high density. Charge density as well as particle density is non-uniform there. A consistent treatment of the Coulomb potential and the particle densities is presented and a peculiar role of the Coulomb potential is elucidated: the physical picture of the Maxwell construction will be effectively recovered. It largely influences the density regime of pasta structures by the charge screening effect.

¹Present address: Research Center for Nuclear Physics (RCNP), Osaka University, Ibaraki, Osaka 567-0047, Japan

1 Introduction

Recently many efforts have been made to reveal “new form of matter” under extreme conditions such as high-temperature and/or high-density. We may find such form through high-energy heavy-ion experiments or observation of compact stars. In this review article we discuss non-uniform structures of cold matter at high density, which is relevant for compact stars. Actually compact stars are good laboratories for nuclear physics and elementary particle physics to study matter at extreme conditions [1, 2, 3, 4].

Nuclear matter in the ground state, which is approximately realized in atomic nuclei, consists of the same number of protons and neutrons and has the density of $\rho_0 \simeq 0.16 \text{ fm}^{-3}$ “the normal nuclear density” or “the saturation density”, and the binding energy of around -16 MeV . This is called “saturation property” of nuclear matter. However, matter in the stellar objects has variety of density and chemical component due to the presence of gravity. In fact, at the surface of neutron stars, there exists a region where the density is lower than ρ_0 over a couple of hundreds meters. The pressure of such matter is retained by degenerate electrons, while baryons are clusterized and have little contribution to the pressure. Due to the gravity the pressure and the density increase in the inner region (in fact, the density at the center amounts to several times the normal nuclear density). Charge neutral matter consists of neutrons and the same number of protons and electrons under chemical equilibrium. Since the kinetic energy of degenerate electrons is much higher than that of baryons, the electron fraction (or the proton one) decreases with increase of density and thus neutrons become the main component and seep out from the clusters. In this way baryons come to contribute to the pressure as well as electrons. At a certain density, other components such as hyperons and strange mesons may emerge. For example, negative kaon condensation, expected to be of a first-order phase transition (FOPT), remarkably softens the equation of state of matter. At even higher density, hadron-quark deconfinement transition may occur and quarks in hadrons are liberated. This phase transition is also considered to be of first-order.

If we assume uniform matter, a FOPT brings about a thermodynamical instability. In other words, matter should have the mixed phase around the critical density. Consider isotherm of water at room temperature for example. At low density (or pressure) water exists in the vapor phase. With increase of density (or pressure), droplets of water appear in the vapor phase. Finally all the volume is filled with liquid water at a certain density (or pressure). The equation of state (EOS), i.e. the relation of pressure and density, at low density and high density is given by those of the vapor and liquid phases, respectively. In between, the EOS of the mixed phase is obtained by the Maxwell construction. Required conditions are equalities of chemical potential, temperature and pressure between the vapor and liquid phases.

Phase transitions in nuclear matter are different from that in water. First, nuclear matter consists of two chemically independent components, i.e. baryons and electrons. Then the equalities of both baryon and electron chemical po-

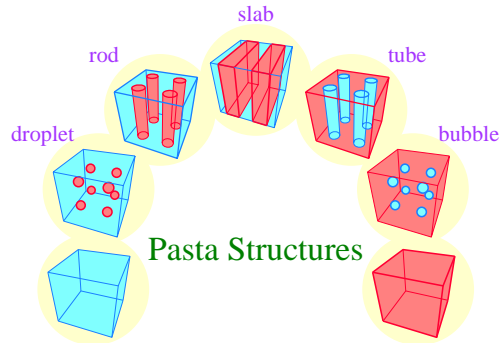


Figure 1: Schematic picture of pasta structures. Phase transition from blue phase (left-bottom) to red phase (right-bottom) is considered.

tentials between two phases are required by the Gibbs conditions in the mixed phase. Therefore the EOS of the mixed phase cannot be obtained simply by the Maxwell construction, which is relevant only for single component. Secondly, those components are electrically charged and the mixed phase is no more uniform. This point is important to the geometrical structure of the mixed phase. In the case of the mixed phase of electrically neutral particles, each phase has arbitrary geometry when surface tension is negligible or two phases are separated when the surface tension is strong. On the other hand the mixed phase in nuclear matter should possess some specific size and shape due to the balance between the surface tension and the Coulomb interaction. To minimize the surface energy plus the Coulomb energy, matter is expected to form a structured mixed phase, i.e. a lattice of lumps of a phase with a geometrical symmetry embedded in the other phase.

At very low densities, nuclei in matter are expected to form the Coulomb lattice embedded in the electron sea, that minimizes the Coulomb interaction energy. With increase of density, “nuclear pasta” structures (see Fig. 1) emerge as a structured mixed phase [5] in the liquid-gas phase transition, where stable nuclear shape may change from droplet to rod, slab, tube, and to bubble. Pasta nuclei are eventually dissolved into uniform matter at a certain nucleon density below the saturation density $\rho_0 \simeq 0.16 \text{ fm}^{-3}$. The name “pasta” comes from rod and slab structures figuratively spoken as “spaghetti” and “lasagna”. Such low-density nuclear matter exists in the collapsing stage of supernovae and in the crust of neutron stars. Supernova matter is relevant to liquid-gas transition of non-beta-equilibrium nuclear matter with a fixed proton mixing ratio and the low-density neutron star matter is relevant to neutron-drip transition of beta-equilibrium nuclear matter.

The appearance of the pasta structures could have important consequences

for the various neutron star phenomena or supernova. If they appear at an early stage of the neutron star evolution nuclear pasta structures could cause a drastic change of the neutrino opacity [6], and consequently influence the subsequent neutron star cooling [7, 8, 9]. It may also affect the matter resistance to the stress and consequently the glitch phenomena [10], etc.

A number of authors have investigated the low-density nuclear matter using various models [5, 11, 12, 13, 14, 15, 16, 17, 18, 19]. Roughly speaking, the favorable nuclear shape is determined by a balance between the surface and Coulomb energies. In most of the previous studies the rearrangement effect of the density profile of the charged particles due to the Coulomb interaction has been discarded. In Ref. [20] the electron screening effect has been studied and it has been found that this effect is of minor importance. However, the rearrangement of the proton profiles as the consequence of the Coulomb repulsion was not shown up in their model. The structured mixed phase is also expected in the phase transitions at higher density, like kaon condensation and hadron-quark phase transition. In these cases, the charge screening effect may be important because the local charge density can be significantly high.

As it was argued in a number of works, the FOPT to a K^- condensate state might occur in neutron stars at densities several times larger than the nuclear saturation density ρ_0 (see [21, 22, 23, 24, 25, 26, 27, 28, 29, 30, 31, 32, 33] and refs therein). Refs [21, 22, 23, 24, 26, 27, 28, 29, 30, 31, 32] and many other studied possibility of the s -wave kaon condensation, whereas refs [25, 33] studied different possibilities for the p -wave condensation. It was concluded that the kaon condensation in neutron stars may indeed occur and it is the FOPT. Such phenomena would lead to interesting consequences in the physics of neutron stars: softening of EOS may give a possibility of the delayed collapse of protoneutron stars to the low-mass black holes, and the nucleon Urca process under background kaons may give a fast cooling mechanism of neutron stars [24, 32, 34, 35, 36, 37, 38, 39]. Kaon condensation as a FOPT may also lead to an expected existence of a wide region of the mixed phase, as was suggested in earlier works, cf. [28, 29, 30], which consists of kaon condensed phase (dense phase) and usual nuclear matter (dilute phase) with some geometrical structures (*kaonic pasta*).

Next we consider the hadron-quark mixed phase. Within the currently accepted theory, the deconfinement transition is believed to occur in hot and/or high-density matter, although its mechanism is not yet well understood. Many people have studied this transition with model calculations and first-principle calculations, like lattice QCD [40]. Above the critical temperature and/or density, the quarks inside each hadron are liberated, and we can understand the resulting situation as quark matter interacting through gluon exchange. Theoretically, static and dynamic properties of quark matter have been extensively studied for quark-gluon plasmas (QGP), color superconductivity [41, 42] and magnetism [43, 44, 45]. Experimentally, evidence of quark matter has been searched for in relativistic heavy-ion collisions (RHIC) [46, 47] and in relics of the early universe and in compact stars [3, 4, 48, 49].

Because many theoretical calculations have suggested that the deconfine-

ment transition should be of first order in the low temperature, high density regime [50, 51], we assume it to be a first-order phase transition. If the deconfinement transition is of first order, it is natural to believe that in the phase transition the system is in a mixed phase. Actually, the hadron-quark mixed phase has been considered during hadronization in RHIC [52, 53, 54] and in the transition region from hadron matter to quark matter in neutron stars [55, 56, 57, 58].

Our purpose here is to investigate low-density nuclear pasta structure, kaonic pasta structure, and hadron-quark pasta structure self-consistently within the mean-field approximation. In particular, we figure out how the charge screening effects modify the results obtained disregarding these effects in a self-consistent manner.

This review article is organized as follows. In Sec. 2, investigations on the mixed phase is reviewed. In Sec. 3 and 4, the nuclear pasta structure in low-density nucleon matter and the kaonic pasta structure at higher densities are studied. Then the finite-size effects on the pasta structures are discussed in Sec. 5. In Sec. 6 and 7, pasta structures in hadron-quark phase transition and the charge-screening effects are discussed. Finally, summary and concluding remarks are given in Sec. 8.

2 General remarks about the treatment of the mixed phases

2.1 Bulk calculation and the finite-size effects

Consider the mixed phase composed of two different phases denoted by I and II. Then the Gibbs conditions require the pressure balance and the equality of the chemical potentials between two phases for phase equilibrium [59].² For a multi-component system with more than one chemical potential, as is common in neutron-star matter, we must impose the equality condition for each chemical potential in order to fulfill the condition of the physico-chemical equilibrium. More definitely, we hereafter consider the charge chemical potential (μ_Q) and the baryon-number chemical potential (μ_B) respecting two conservation laws in neutron-star matter: $\mu_Q^I = \mu_Q^{II}$ and $\mu_B^I = \mu_B^{II}$. On the other hand, the first condition is not fulfilled in the Maxwell construction, since the *local* charge neutrality is implicitly imposed, while only the *global* charge neutrality must be satisfied.

A naive application of the Gibbs conditions to the mixed phase composed of two semi-infinite matter, when one ignores the surface and Coulomb interaction, demonstrates a broad region of the structured mixed phase (SMP), cf. [29, 60]. However the charge screening effect (caused by the non-uniform charged particle distributions) should be very important when the typical structure size is of the order of the minimal Debye screening length in the problem. It may largely

²We consider here matter at zero temperature

affect the stability condition of the geometrical structures in the mixed phases.

We shall see that the Debye screening effects greatly modify the mechanical stability of SMP, and consequently largely limit the density region of the mixed phase. In the absence of SMP we effectively recover the picture of phase equilibrium given by the Maxwell construction where two bulk phases are separated without spoiling the Gibbs conditions.

Consider SMP consisting of two phases I and II, where we assume spherical droplets of phase I with a radius R to be embedded in the matter of phase II and two phases are clearly separated by sharp boundaries. We divide the whole space into the equivalent Wigner-Seitz cells with a radius R_W (see Fig. 2). The volume of the cell is $V_W = 4\pi R_W^3/3$ and that of the droplet is $V = 4\pi R^3/3$.

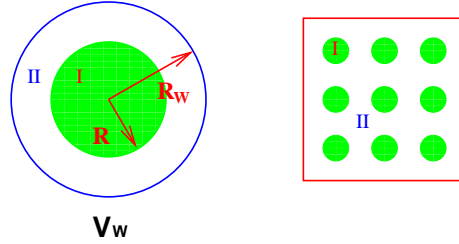


Figure 2: Equal droplets made of the phase I embedded in the phase II (right panel), and the geometrical structure of the Wigner-Seitz cell (left panel)

A bulk calculation proceeds as follows [57]. First, consider two semi-infinite matter with a volume fraction f_V , separated by a sharp boundary. By applying the global charge-neutrality condition and the pressure balance condition under the chemical equilibrium, we can get f_V for each density. Then we use the volume fraction thus determined to describe the geometrical structure in each Wigner-Seitz cell. For a given volume fraction $f_V = (R/R_W)^3$, the total energy E may be written as the sum of the volume energy E_V , the Coulomb energy E_C and the surface energy E_S ,

$$E = E_V + E_C + E_S. \quad (1)$$

We further assume, for simplicity, that baryon number (ρ_B^α) and charge (ρ_{ch}^α) densities are uniform in each phase α , $\alpha = \text{I, II}$ as in semi-infinite matter. Then, E_V can be written as $E_V/V_W = f_V \epsilon^{\text{I}}(\rho_B^{\text{I}}) + (1 - f_V) \epsilon^{\text{II}}(\rho_B^{\text{II}})$ in terms of the energy densities ϵ^α , $\alpha = \text{I, II}$. The surface energy E_S may be represented as $E_S/V_W = f_V \times 3\tau/R$ in terms of the surface tension τ . The Coulomb energy E_C is given by

$$E_C/V_W = f_V \times \frac{16\pi^2}{15} (\rho_{ch}^{\text{I}} - \rho_{ch}^{\text{II}})^2 R^2. \quad (2)$$

The optimal value of R , which we call R_D , is determined by the minimum condition,

$$\left. \frac{\partial(E/V_W)}{\partial R} \right|_{R=R_D} = 0, \quad (3)$$

for a given f_V (see Fig. 3). Since E_V does not depend on R , we can *always* find a minimum as a result of the competition between the Coulomb and the surface energies, satisfying the well-known relation, $E_S = 2E_C$. However, such

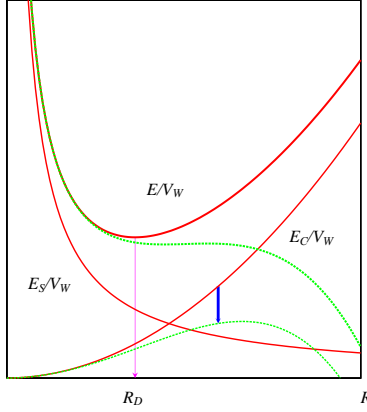


Figure 3: Schematic view of the total energy and each contribution in the bulk calculations (solid curves). Screening effect reduces the Coulomb energy, shown by the thick arrow.

bulk calculations have been proved to be too crude for the discussions of SMP. Instead, a careful consideration of the interface of two phases is required. As a defect of the bulk calculations they ignore the *finite-size effects*. In particular, they have the inconsistent treatment of the Coulomb potential; they do not use the Poisson equation, so that the charge density profiles are assumed ab initio to be uniform and the Coulomb potential is assumed to be $1/r$. If one properly solves the Poisson equation, one should have the screening effect as a result of the rearrangement of the charge-density distribution. Hence, the radius R_D should be not too large compared with the Debye screening length λ_D ,

$$\lambda_D^{-2} = \sum_i (\lambda_D^i)^{-2}, \quad (4)$$

$$1/\lambda_D^i{}^2 = 4\pi \frac{\partial \rho_Q}{\partial \mu_i}, \quad (5)$$

in order the above treatment to be justified, the suffix i runs over the particle species. Otherwise, the Coulomb energy is reduced by the charge screening effect, which should lead to a *mechanical instability* of SMP in some cases (Fig. 3).

We have been recently exploring the effect of the charge screening in the context of the various structured mixed phases [61, 62, 63, 64, 65, 66]. In fact, we have examined the mixed phase at the hadron-quark transition, kaon condensation and of nuclear pasta, and found that in cases of the hadron-quark transition and kaon condensation the mixed phase might be largely limited

by the charge screening and surface effects. In the case of the hadron-quark deconfinement transition, for example, $\lambda_D^q \simeq 5$ fm and λ_D^p, λ_D^e are of the same order as λ_D^q , for a typical density with $\mu_B \simeq 1$ GeV. We shall see in the following that R_D is typically of the same order as $\lambda_D \sim \lambda_D^q$, and the mechanical stability of the droplet is much affected by the screening effect.

Besides the screening effect, note that the surface tension and the pressure balance condition are inconsistently incorporated in the bulk calculations; actually the pressure balance condition is imposed before introducing the surface tension.

2.2 Gauge invariance and the meaning of chemical potentials

When we use the idea of the density functional theory [67, 68], the thermodynamic potential is given as a functional of the particle densities $\rho_i(\mathbf{r})$,

$$\Omega(\rho_i(\mathbf{r})) = \int d^3r \epsilon_{\text{kin+str}}(\rho_i(\mathbf{r})) + E_V - \sum_i \mu_i \int d^3r \rho_i(\mathbf{r}), \quad (6)$$

where μ_i are the chemical potentials and $\epsilon_{\text{kin+str}}$ stands for the contributions of the kinetic energy and the strong interaction energy. The Coulomb interaction energy E_V is also expressed in terms of particle densities,

$$E_V = \frac{1}{2} \sum_{i,j} \int d^3r d^3r' \frac{Q_i \rho_i(\mathbf{r}) Q_j \rho_j(\mathbf{r}')}{|\mathbf{r} - \mathbf{r}'|}, \quad (7)$$

with Q_i being the particle charge ($Q = -e < 0$ for the electron). Then the chemical potentials are given as

$$\mu_i = \frac{\partial \epsilon_{\text{kin+str}}}{\partial \rho_i} - N_i^{\text{ch}} V(\mathbf{r}), \quad N_i^{\text{ch}} = Q_i/e, \quad (8)$$

with the electric potential $V(\mathbf{r})$:

$$V(\mathbf{r}) = - \sum_i \int d^3r' \frac{e Q_i \rho_i(\mathbf{r}')}{|\mathbf{r} - \mathbf{r}'|} \quad (9)$$

generated by the particle distributions.

We must keep the gauge invariance through the calculation: V can be arbitrarily shifted by a constant V_0 , $V(\mathbf{r}) \rightarrow V(\mathbf{r}) - V_0$. Formally varying Eq. (8) with respect to $V(\mathbf{r})$ or μ_i we have the matrix form relation,

$$A_{ij} \frac{\partial \rho_j}{\partial V} = N_i^{\text{ch}}, \quad A_{ij} B_{jk} = \delta_{ik}, \quad (10)$$

where matrices A and B are defined as

$$A_{ij} \equiv \frac{\delta^2 E_{\text{kin+str}}}{\delta \rho_i \delta \rho_j}, \quad B_{ij} \equiv \frac{\partial \rho_i}{\partial \mu_j}. \quad (11)$$

Eqs. (10) and (11) reproduce the gauge-invariance relation,

$$\frac{\partial \rho_i}{\partial V} = N_j^{\text{ch}} \frac{\partial \rho_j}{\partial \mu_i}, \quad (12)$$

clearly showing that constant-shift of the chemical potential is compensated by the gauge transformation of $V(\mathbf{r})$: $\mu_i \rightarrow \mu_i + N_i^{\text{ch}} V_0$, as $V(\mathbf{r}) \rightarrow V(\mathbf{r}) - V_0$. Hence chemical potential μ_i acquires physical meaning only after fixing the gauge of $V(\mathbf{r})$.

We reconsider the relation between the Gibbs conditions and the Maxwell construction from this view point. Consider a schematic situation for simplicity, where two semi-infinite matter denoted by I and II are separated by a sharp boundary. As has been mentioned, at first glance the Maxwell construction apparently violates the Gibbs conditions, especially the equilibrium condition for the charge chemical potential $\mu_Q (= \mu_e)$ in our context. However, correctly speaking, when we say $\mu_e^{\text{I}} \neq \mu_e^{\text{II}}$ within the Maxwell construction, it means nothing but the difference in the electron number density ρ_e in two phases, $\rho_e^{\text{I}} \neq \rho_e^{\text{II}}$; this is simply because $\rho_e = \mu_e^3 / (3\pi^2)$, if the Coulomb potential is *absent*. Once the Coulomb potential is taken into account, using Eq. (8), ρ_e can be written as

$$\rho_e = \frac{(\mu_e - V)^3}{3\pi^2}. \quad (13)$$

Thus we may have $\mu_e^{\text{I}} = \mu_e^{\text{II}}$ and $\rho_e^{\text{I}} \neq \rho_e^{\text{II}}$ simultaneously, with the *different values of V* , $V^{\text{I}} \neq V^{\text{II}}$ (see Fig. 4). We shall see that if the Coulomb interaction

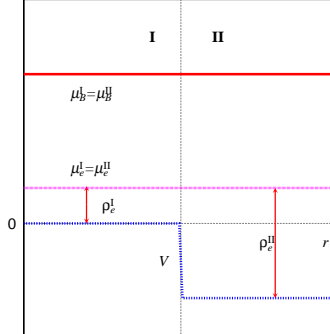


Figure 4: Relation between the charge chemical potential $\mu_Q (= \mu_e)$ and the electron number density ρ_e in the presence of the Coulomb potential V . Fulfilling the Gibbs conditions, $\mu_B^{\text{I}} = \mu_B^{\text{II}}$, $\mu_e^{\text{I}} = \mu_e^{\text{II}}$, we can change ρ_e in two phases as in the Maxwell construction, if V suitably changes from one phase to another.

is properly taken into account, the resultant EOS looks similar to that given by the Maxwell construction.

3 Low-density nuclear pasta structures

3.1 Relativistic mean-field (RMF) treatment of nucleon matter

Here we explain how to investigate the property of nuclear matter at low density. Exploiting the idea of the density functional theory within the RMF model, we can formulate equations of motion to study non-uniform nuclear matter numerically, cf. [67, 68]. The RMF model with fields of mesons and baryons introduced in a Lorentz-invariant way is not only relatively simple for numerical calculations, but also sufficiently realistic to reproduce bulk properties of finite nuclei as well as the saturation properties of nuclear matter [69]. In our framework, the Coulomb interaction is properly included in the equations of motion for nucleons and electrons and for meson mean fields, and we solve the Poisson equation for the Coulomb potential V self-consistently with those equations. Thus the baryon and electron density profiles, as well as the meson mean fields, are determined in a fully consistent way with the Coulomb interaction.

3.1.1 Thermodynamic potential and the equations of motion

We start with the thermodynamic potential for the system of neutrons, protons, electrons and mesons including kaons

$$\Omega = \Omega_N + \Omega_M + \Omega_e. \quad (14)$$

The first term

$$\Omega_N = \sum_{a=p,n} \int d^3r \left[\int_0^{k_{F,a}} \frac{d^3k}{4\pi^3} \sqrt{m_N^{*2} + k^2} - \rho_a \nu_a \right] \quad (15)$$

is the contribution of nucleons with the local Fermi momenta $k_{F,a}(\mathbf{r})$; $a = n, p$, $m_N^*(\mathbf{r}) = m_N - g_{\sigma N} \sigma(\mathbf{r})$ is the effective nucleon mass and m_N is the nucleon mass in the vacuum. Nucleons couple with σ , ω and ρ mesons and thereby,

$$\begin{aligned} \nu_n(\mathbf{r}) &= \mu_n - g_{\omega N} \omega_0(\mathbf{r}) + g_{\rho N} R_0(\mathbf{r}), \\ \nu_p(\mathbf{r}) &= \mu_p + V(\mathbf{r}) - g_{\omega N} \omega_0(\mathbf{r}) - g_{\rho N} R_0(\mathbf{r}), \end{aligned} \quad (16)$$

where μ_n and μ_p are neutron and proton chemical potentials and $g_{\sigma N}$, $g_{\omega N}$ and $g_{\rho N}$ are coupling constants between corresponding fields.

The second term in (14) incorporates the scalar (σ) and vector (ω_0, R_0) mean fields,

$$\begin{aligned} \Omega_M &= \int d^3r \left[\frac{(\nabla \sigma)^2 + m_\sigma^2 \sigma^2}{2} + U(\sigma) \right. \\ &\quad \left. - \frac{(\nabla \omega_0)^2 + m_\omega^2 \omega_0^2}{2} - \frac{(\nabla R_0)^2 + m_\rho^2 R_0^2}{2} \right], \end{aligned} \quad (17)$$

Table 1: Parameter set used in RMF in our calculation.

$g_{\sigma N}$	$g_{\omega N}$	$g_{\rho N}$	b	c	m_{σ}	m_{ω}	m_{ρ}
6.3935	8.7207	4.2696	0.008659	0.002421	400 MeV	783 MeV	769 MeV

where m_{σ} , m_{ω} and m_{ρ} are the field masses, and $U(\sigma) = \frac{1}{3}bm_N(g_{\sigma N}\sigma)^3 + \frac{1}{4}c(g_{\sigma N}\sigma)^4$ is the nonlinear potential for the scalar field.

The third term in (14) contains the contribution of the Coulomb field (described by the potential $V(\mathbf{r})$) and the contribution of relativistic electrons,

$$\Omega_e = \int d^3r \left[-\frac{1}{8\pi e^2}(\nabla V)^2 - \frac{(\mu_e - V)^4}{12\pi^2} \right], \quad (18)$$

where μ_e is the electron chemical potential.

Temperature T is kept to be zero in the present study.

For nucleons and electrons we used the local-density approximation, i.e., nucleons and electrons are described by their local densities. This approximation has its sense only if the typical length of the change of the nucleon density is larger than the inter-nucleon distance. Derivative terms of the particle densities can be incorporated in the quasi-classical manner by the derivative expansion within the density functional theory [67, 68]. Their contribution to the energy can be reduced to a surface tension term. Here we simply discard those derivative terms, as a first-step approximation. Thus we discard the contribution of the nucleon fields to the surface tension assuming that it is smaller than the corresponding contribution of the meson fields that we retain. In the case when we suppress derivative terms of the nucleon densities they follow changes of the meson σ , ω , ρ mean fields and the Coulomb fields that have derivative terms. Note that we have fitted our model to properly describe finite nuclei (see below) without including nucleon derivative terms. If we introduced them it would need to re-adjust the model parameters. We should bear in mind that for small structure sizes quantum effects become prominent. For simplicity we disregard these effects. Thus we may properly describe only rather large-size structures within this scheme.

3.1.2 Equations of motion and numerical procedure

Equations of motion for the mean fields and for the Coulomb potential are obtained from the variational principle: $\frac{\delta\Omega}{\delta\phi_i(\mathbf{r})} = 0$ ($\phi_i = \sigma, \omega_0, R_0, V$),

$$\nabla^2\sigma(\mathbf{r}) = m_{\sigma}^2\sigma(\mathbf{r}) + \frac{dU}{d\sigma} - g_{\sigma N}(\rho_n^s(\mathbf{r}) + \rho_p^s(\mathbf{r})), \quad (19)$$

$$\nabla^2\omega_0(\mathbf{r}) = m_{\omega}^2\omega_0(\mathbf{r}) - g_{\omega N}(\rho_p(\mathbf{r}) + \rho_n(\mathbf{r})), \quad (20)$$

$$\nabla^2 R_0(\mathbf{r}) = m_\rho^2 R_0(\mathbf{r}) - g_{\rho N}(\rho_p(\mathbf{r}) - \rho_n(\mathbf{r})), \quad (21)$$

$$\nabla^2 V(\mathbf{r}) = 4\pi e^2 \rho_{\text{ch}}(\mathbf{r}), \quad (22)$$

with the proton and neutron scalar densities

$$\rho_a^s(\mathbf{r}) = \int_0^{k_{\text{F},a}(\mathbf{r})} \frac{d^3 k}{4\pi^3} \frac{m_N^*(\mathbf{r})}{\sqrt{m_N^*(\mathbf{r})^2 + k^2}}, \quad (a = p, n), \quad (23)$$

and the charge density

$$\rho_{\text{ch}}(\mathbf{r}) = \rho_p(\mathbf{r}) - \rho_e(\mathbf{r}). \quad (24)$$

For nucleons and electrons, $\frac{\delta\Omega}{\delta\rho_a(\mathbf{r})} = 0$ ($a = n, p, e$) give the expressions of the chemical potentials;

$$\mu_e = (3\pi^2 \rho_e(\mathbf{r}))^{1/3} + V(\mathbf{r}), \quad (25)$$

$$\begin{aligned} \mu_n = \mu_B = & \sqrt{k_{\text{F},n}(\mathbf{r})^2 + m_N^*(\mathbf{r})^2} \\ & + g_{\omega N} \omega_0(\mathbf{r}) - g_{\rho N} R_0(\mathbf{r}), \end{aligned} \quad (26)$$

$$\begin{aligned} \mu_p = \mu_B - \mu_e = & \sqrt{k_{\text{F},p}(\mathbf{r})^2 + m_N^*(\mathbf{r})^2} \\ & + g_{\omega N} \omega_0(\mathbf{r}) + g_{\rho N} R_0(\mathbf{r}) - V(\mathbf{r}). \end{aligned} \quad (27)$$

The last two equations are the standard relations between the local nucleon densities and chemical potentials. We have assumed that the system is in the chemical equilibrium with respect to the weak, electromagnetic and strong interactions and we introduced the baryon chemical potential $\mu_B = \mu_n$ and the charge chemical potential, i.e. the electron chemical potential, μ_e , according to the corresponding conserved charges.

To solve the above coupled equations numerically, the whole space is divided into equivalent Wigner-Seitz cells with a radius R_W . The geometrical shape of the cell changes as follows: sphere in three-dimensional (3D) calculation, cylinder in 2D and slab in 1D, respectively. Each cell is globally charge-neutral and all physical quantities in the cell are smoothly connected to those of the next cell with zero gradients at the boundary. Every point inside the cell is represented by the grid points (number of grid points $N_{\text{grid}} \approx 100$) and differential equations for fields are solved by the relaxation method for a given baryon-number density under constraints of the global charge neutrality. Details of the numerical procedure are explained in Ref. [69]. To fix the gauge of $V(\mathbf{r})$, we choose the following condition as

$$V(R_W) = 0. \quad (28)$$

3.1.3 Parameter set and finite nuclei

Parameters of the RMF model are chosen to reproduce saturation properties of symmetric nuclear matter: the minimum energy per nucleon -16.3 MeV at $\rho = \rho_0 \equiv 0.153 \text{ fm}^{-3}$, the incompressibility $K(\rho_0) = 240$ MeV, the effective

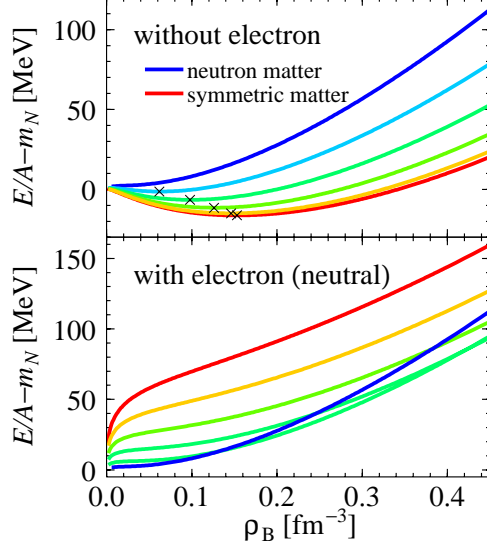


Figure 5: EOS of uniform nucleon matter with different proton mixing ratios. Red line indicates symmetric matter (proton mixing ratio $Y_p = 0.5$) and blue line indicates neutron matter ($Y_p = 0$). Lines with intermediate colors show the case of $Y_p = 0.4, 0.3, 0.2$ and 0.1 . Crosses on the lines show the minimum points. Upper panel is the case without electron and the Coulomb energy, while the lower panel is the case of charge-neutral matter which includes energy of electrons.

nucleon mass $m_N^*(\rho_0) = 0.78m_N$; $m_N = 938$ MeV, and the isospin-asymmetry coefficient $a_{\text{sym}} = 32.5$ MeV. Coupling constants and meson masses used in our calculation are listed in Table 1. Figure 5 shows the binding energy per nucleon of uniform nucleon matter. The proton mixing ratio Y_p is the number ratio of protons (Z) to total baryons (A), $Y_p = Z/A$. The saturation property mentioned above is seen for symmetric nuclear matter ($Y_p = 0.5$) in the upper panel of Fig. 5. Note that if one imposes the charge neutrality by inclusion of electrons, the saturation property cannot be seen (lower panel of Fig. 5).

For the study of non-uniform nuclear matter, the ability to reproduce the bulk properties of finite nuclei should be essential. We check how it works to describe finite nuclei. In this calculation, for simplicity, we assume the spherical shape of nuclei. The electron density is set to be zero. Therefore, neither the global charge neutrality condition nor the local charge-neutrality condition is imposed.

In Fig. 6 (left panel) we show the density profiles of some typical nuclei. One can see how well our framework may reproduce the density profiles. To get a still better fit, especially around the surface region, we might need to include

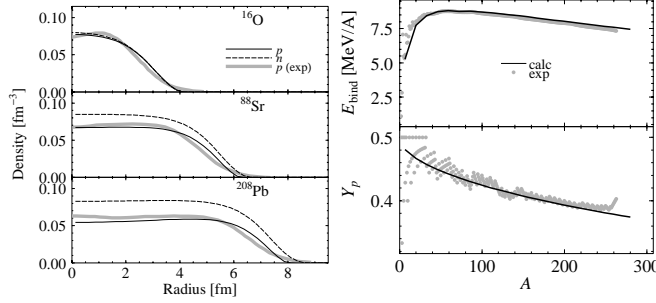


Figure 6: Properties of finite nuclei obtained with the present RMF model. Left: the density profiles of typical nuclei. The proton number densities (solid curves) are compared with the experimental data. Right: binding energy per nucleon $-(E/A - m_N)$ and the proton mixing ratio Y_p of finite nuclei.

the derivative terms of the nucleon densities, as we have already remarked. Fine structures seen in the empirical density profiles, which may come from the shell effects (see, e.g., a proton density dip at the center of a light ^{16}O nucleus), cannot be reproduced by the mean-field theory. The effect of the rearrangement of the proton density distribution is seen in heavy nuclei. Protons repel each other, which enhances their density near the surface of heavy nuclei. This effect is analogous to the charge screening effect for the Coulomb potential in a sense that the proton distribution is now changed not on the scale of the nuclear radius, but on another length scale, that we will call the proton Debye screening length (see Eq. (30) below). It gives rise to important consequences for the pasta structures since the proton Debye screening length is typically less than the lump size. The optimal value of the proton mixing ratio Y_p is obtained by imposing the beta-equilibrium condition for a given baryon number. Figure 6 (right panel) shows the baryon-number dependence of the binding energy per baryon E_{bind} and the proton mixing ratio Y_p . We can see that the bulk properties of finite nuclei (density, binding energy, and proton to baryon number ratio) are satisfactorily reproduced for our present purpose.

Note that in our framework we must use a sigma mass $m_\sigma = 400$ MeV [70], a slightly smaller value than that one usually uses, to get an appropriate fit. If we used a popular value $m_\sigma \approx 500$ MeV, finite nuclei would be over-bound by about 3 MeV/A. The actual value of the sigma mass (as well as the omega and rho masses) has little relevance for the case of infinite nucleon matter, since it enters the thermodynamic potential only in the combination $\tilde{C}_\sigma = g_{\sigma N}/m_\sigma$. However meson masses are important characteristics of finite nuclei and of other non-uniform nucleon systems, like those in pasta. The effective meson mass characterizes the typical scale for the spatial change of the meson field and consequently it affects the value of the effective surface tension.

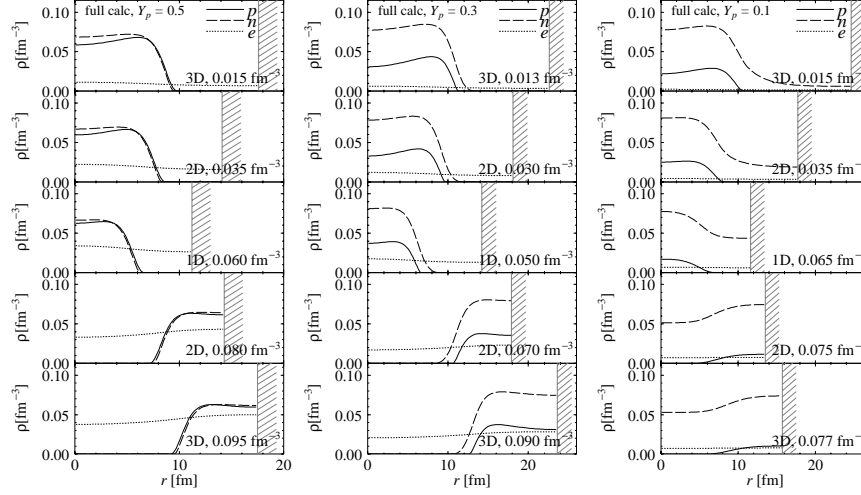


Figure 7: Examples of the density profiles in the cell for symmetric nuclear matter with $Y_p=0.5$ (left panel) and for asymmetric matter with $Y_p = 0.3$ (center panel) and 0.1 (right panel).

3.2 Nucleon matter at fixed proton mixing ratios

First, we concentrate on the discussion of the behavior of nucleon matter at fixed values of the proton mixing ratio Y_p . Particularly, we explore the proton mixing ratios $Y_p = 0.1, 0.3$, and 0.5 . The cases $Y_p = 0.3 - 0.5$ should be relevant for supernova matter and for newly born neutron stars. Figure 7 shows some typical density profiles inside the Wigner-Seitz cells. The geometrical dimension of the cell is denoted as “3D” (three-dimensional sphere), etc. The horizontal axis in each panel denotes the radial distance from the center of the cell. The cell boundary is indicated by the hatch. From the top to the bottom the configuration corresponds to droplet (3D), rod (2D), slab (1D), tube (2D), and bubble (3D). The nuclear “pasta” structures are clearly manifested. For the lowest Y_p case ($Y_p = 0.1$), the neutron density is finite at any point: the space is filled by dripped neutrons. The value of Y_p above which neutrons drip is around 0.26 in our 3D calculation, for example. For a higher Y_p , the neutron density drops to zero outside the nucleus. The proton number density always drops to zero outside the nucleus. We can see that the charge screening effects are pronounced. Due to the spatial rearrangement of electrons the electron density profile becomes no more uniform. This non-uniformity of the electron distribution is more pronounced for a higher Y_p and a higher density. Protons repel each other. Thereby the proton density profile substantially deviates from the step-function. The proton number is enhanced near the surface of the lump.

The equation of state (EOS) for the sequence of geometric structures is shown in Fig. 8 (top panels) as a function of the averaged baryon-number density. Note that the energy $E/A - m_N$ also includes the kinetic energy of

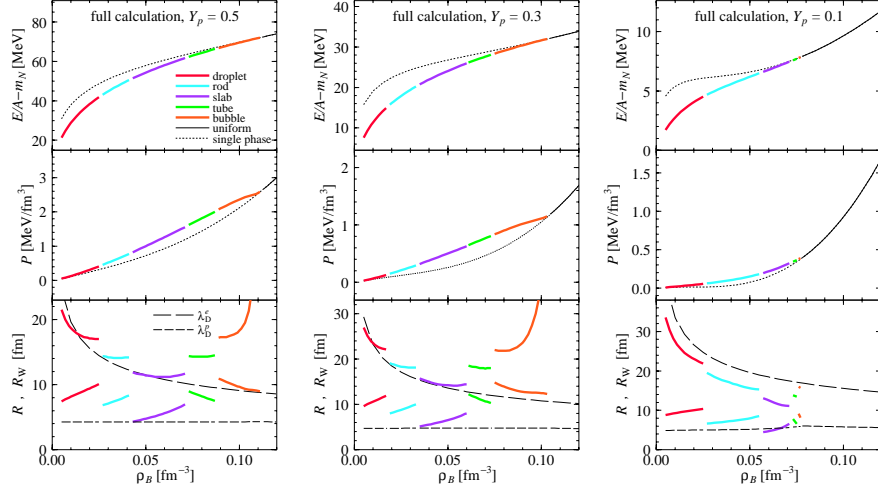


Figure 8: Binding energy per nucleon (top), pressure (middle), and the cell and lump sizes (bottom) for symmetric nuclear matter with $Y_p=0.5$ (left panel), and for asymmetric matter with $Y_p = 0.3$ (center panel) and 0.1 (right panel).

electrons, which makes the total pressure positive (middle panels). The lowest-energy configurations are selected among various geometrical structures. The most favorable configuration changes from the droplet to rod, slab, tube, bubble, and to the uniform one (the dotted thin curve) with an increase of density. The appearance of non-uniform structures in matter results in a softening of EOS: the energy per baryon gets lower up to about 15 MeV/A compared to uniform matter.

The bottom panels in Fig. 8 are the cell radii R_W and the lump radii R versus averaged baryon number density. The radius R is defined by way of a density fluctuation as

$$R = \begin{cases} R_W \frac{\langle \rho_p \rangle^2}{\langle \rho_p^2 \rangle}, & (\text{for droplet, rod, and slab}) \\ R_W \left(1 - \frac{\langle \rho_p \rangle^2}{\langle \rho_p^2 \rangle} \right), & (\text{for tube and bubble}) \end{cases} \quad (29)$$

where the bracket “ $\langle \rangle$ ” indicates the average along the radial (for 3D and 2D cases) or perpendicular (1D) direction in the cell. Dashed curves show the Debye screening lengths of electrons and protons calculated as

$$\lambda_D^a = \left(4\pi e^2 \frac{d\rho_a^{\text{av}}}{d\mu_a} \right)^{-1/2} \quad (a = p, e), \quad (30)$$

where ρ_p^{av} is the proton number density averaged inside the nucleus (the region with finite ρ_p) and ρ_e^{av} is the electron density averaged inside the cell. Actually

doing more carefully we should introduce four Debye screening lengths $\lambda_D^{a,<}$ and $\lambda_D^{a,>}$ with a separate averaging for the interior and the exterior of the nuclei. However we observe that the proton number density is always zero in the exterior region and $\lambda_D^{p,>} = \infty$ thereby. For electrons $\lambda_D^{e,<}$ and $\lambda_D^{e,>}$ are in general different but both being large and of the same order of magnitude in the pasta case under consideration. Therefore we actually do not need a more detailed analysis of these quantities. Note that these values are obviously gauge invariant. Numerically, the cell radii R_W for droplet, rod, and slab configurations at $Y_p = 0.5$ and 0.3 were proven to be close to the electron screening length. For the tube, R_W is larger than λ_D^e . For $Y_p = 0.1$, in all cases R_W is substantially smaller than λ_D^e and the electron screening should be much weaker, thereby. In all cases, except for bubbles (at $Y_p = 0.5$ and 0.3), the structure radii R are smaller than λ_D^e . This means that the Debye screening effect of electrons inside these structures should not be pronounced. For bubbles at $Y_p = 0.5$ and 0.3 , λ_D^e is substantially smaller than the cell size and the electron screening should be significant. For $Y_p = 0.5, 0.3, 0.1$ in all cases (with the only exception $Y_p = 0.1$ for slabs), the value $\lambda_D^{p,<}$ is shorter than R . Hence the density rearrangement of protons is essential for the pasta structures, as it is indeed seen from the Fig. 7.

As we have mentioned one of the characteristics of our calculation is that the obtained density profiles of particles in the cell is free from assumption and is consistent with the potential. However, the usage of Wigner-Seitz cell is a significant limitation. It is because we have to assume the geometrical symmetry. At zero temperature, a specific pasta structure should be the distinct ground state for a given baryon density. However, at a certain density near the boundary of two pasta structures, some intermediate structures could be favorable, or at least can be local-minimum state. Furthermore, intermediate structure should not be negligible at finite temperatures. Such intermediate states and incomplete pasta structures are reported in the studies using molecular dynamics [16, 19, 20, 71, 72]. In fact, molecular dynamics simulation is completely free from assumption of nucleon distribution. However, uniform electron background is assumed and beta-equilibrium condition is not imposed in the molecular dynamics yet. In this sense, the present mean-field calculation and the molecular dynamics for nuclear matter structure are complementary models to each other.

3.3 Nucleon matter in beta equilibrium

Next, we consider neutron star matter at zero temperature, and explore the non-uniform structures for nucleon matter in beta equilibrium. Figure 9 shows the density profiles for different baryon number densities. The droplet structure itself is quite similar to the case of the fixed proton mixing ratio $Y_p = 0.1$ considered above. The apparently different feature in this case is that only the droplet configuration appears as a non-uniform structure. It should be noticed, however, that the presence or absence of the concrete pasta structure sensitively depends on the choice of the effective interaction.

In Fig. 10 we plot the energy per baryon (top), the cell and lump sizes (middle), and the proton number ratio (bottom). The effect of the non-uniform

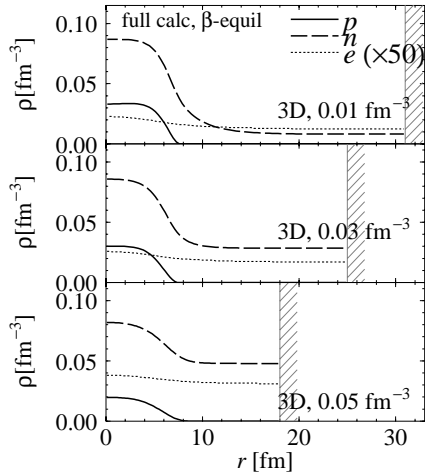


Figure 9: Density profiles in the cell for nuclear matter in beta equilibrium with baryon-number densities, 0.01, 0.03 and 0.05 fm⁻³ from the top to the bottom.

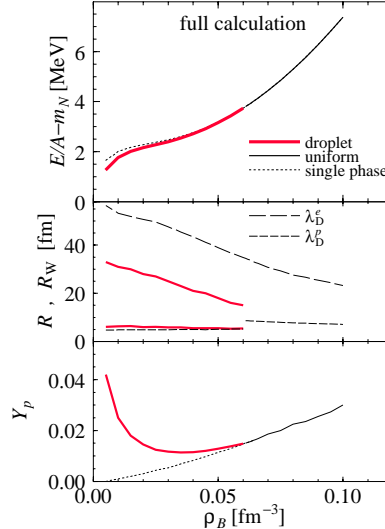


Figure 10: Binding energy (top), cell and lump sizes (middle), and proton mixing ratio (bottom) in the cell for nuclear matter in beta equilibrium.

structure on EOS (the difference between the energy of uniform matter and that of non-uniform one) is small. However, the proton mixing ratio is significantly affected by the presence of the pasta at lower densities. In the zero-density limit, the proton mixing ratio should converge to that of the normal nuclei. The droplet radius and the cell radius in the middle panel of Fig. 10 are always smaller than the electron Debye screening length λ_D^e . Thereby the effect of the electron charge screening is small. Unlike the fixed Y_p cases, the droplet radius is comparable to the proton Debye screening length, which means that the effect of the proton rearrangement is not pronounced in this case. In fact, there is no enhancement of the proton number density near the surface in Fig. 9, in contrast to Fig. 7.

4 Kaonic pasta structures at high densities

Next let us explore high-density nuclear matter in beta equilibrium, which is expected in the inner core of neutron stars.

Kaons are Nambu-Goldstone bosons accompanying the spontaneous breaking of chiral $SU(3) \times SU(3)$ symmetry and the lightest mesons with strangeness. Their effective energy is much reduced by the kaon-nucleon interaction in nuclear medium, which is dictated by chiral symmetry. For low-energy kaons the s -wave interaction is dominant and attractive in the $I = 1$ channel, so that

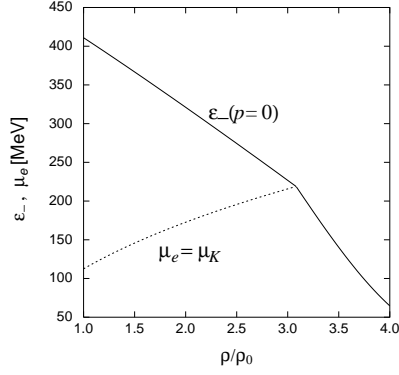


Figure 11: Onset mechanism of kaon condensation within the chiral model.

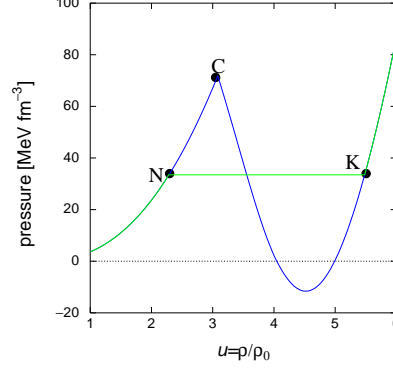


Figure 12: Original EOS and the Maxwell construction given by the chiral model. “C” indicates the critical point between nucleon and kaonic phases in the case of uniform matter (without mixed phase). The mixed phase is given by the Maxwell construction between “N” and “K”.

negatively charged kaons appear in the neutron-rich matter once the process $n \rightarrow p + K^-$ becomes energetically allowed. Since kaons are bosons, they cause the Bose-Einstein condensation at zero momentum [21]. The single-particle energy of kaons is given in a model-independent way (see Appendix):

$$\epsilon_{\pm}(\mathbf{p}) = \sqrt{|\mathbf{p}|^2 + m_K^{*2} + ((\rho_n + 2\rho_p)/4f^2)^2} \pm (\rho_n + 2\rho_p)/4f^2, \quad (31)$$

where m_K^* is the effective mass of kaons, $m_K^{*2} = m_K^2 - \Sigma_{KN}(\rho_n^s + \rho_p^s)/f^2$, with the KN sigma term, Σ_{KN} , and the meson decay constant, $f \equiv f_K \sim f_\pi$. The threshold condition then reads [73]

$$\mu_K = \epsilon_{-}(\mathbf{p} = 0) = \mu_n - \mu_p = \mu_e, \quad (32)$$

which means the kaon distribution function diverges at $\mathbf{p} = 0$ (Fig. 11).

If kaon condensation occurs in nuclear matter, it has many implications on compact stars; one of the interesting possibilities may be the delayed collapse of a protoneutron star to a low-mass black hole due to the large softening of EOS [32, 35], and another one is a fast cooling mechanism of young neutron stars due to the nucleon Urca process under background kaons [36, 37].

Since many studies have shown that kaon condensation is of first order, we must carefully treat the phase change (Fig. 12). In the following we discuss the mixed phase in the phase transition in a similar way to nuclear pasta.

4.1 RMF treatment of nuclear matter with kaon condensation

We explore high-density nuclear matter with kaon condensation by means of RMF model as in low-density matter. Using the same model we can discuss the non-uniform structure of nuclear matter both at low- and high-density regime in an unified way. To incorporate kaons into our RMF calculation, the thermodynamic potential of Eq. (14) is modified as

$$\Omega = \Omega_N + \Omega_M + \Omega_e + \Omega_K, \quad (33)$$

$$\Omega_K = \int d^3r \left\{ -\frac{f_K^2 \theta^2}{2} \left[-m_K^{*2} + (\mu_K - V + g_{\omega K} \omega_0 + g_{\rho K} R_0)^2 \right] + \frac{f_K^2 (\nabla \theta)^2}{2} \right\}, \quad (34)$$

where $m_K^* = m_K - g_{\sigma K} \sigma$, $\mu_K = \mu_e$, and the kaon field $K = f_K \theta / \sqrt{2}$ (f_K is the kaon decay constant). We, hereafter, neglect a rather unimportant term $\propto \sigma^2 \theta^2$.³ The equations of motion are similar to Eqs. (19) - (27) given for the low-density case (Sec. 3). We list here the modified and added ones as

$$\begin{aligned} \nabla^2 \sigma(\mathbf{r}) = & m_\sigma^2 \sigma(\mathbf{r}) + \frac{dU}{d\sigma} - g_{\sigma N}(\rho_n^s(\mathbf{r}) + \rho_p^s(\mathbf{r})) \\ & + 2g_{\sigma K} m_K f_K^2 \theta^2(\mathbf{r}), \end{aligned} \quad (35)$$

$$\begin{aligned} \nabla^2 \omega_0(\mathbf{r}) = & m_\omega^2 \omega_0(\mathbf{r}) - g_{\omega N}(\rho_p(\mathbf{r}) + \rho_n(\mathbf{r})) \\ & - f_K^2 g_{\omega K} \theta^2(\mathbf{r}) [\mu_K - V(\mathbf{r}) + g_{\omega K} \omega_0(\mathbf{r}) + g_{\rho K} R_0(\mathbf{r})], \end{aligned} \quad (36)$$

$$\begin{aligned} \nabla^2 R_0(\mathbf{r}) = & m_\rho^2 R_0(\mathbf{r}) - g_{\rho N}(\rho_p(\mathbf{r}) - \rho_n(\mathbf{r})) \\ & - f_K^2 g_{\rho K} \theta^2(\mathbf{r}) [\mu_K - V(\mathbf{r}) + g_{\omega K} \omega_0(\mathbf{r}) + g_{\rho K} R_0(\mathbf{r})], \end{aligned} \quad (37)$$

$$\begin{aligned} \nabla^2 \theta(\mathbf{r}) = & \left[m_K^{*2}(\mathbf{r}) - (\mu_K - V(\mathbf{r})) \right. \\ & \left. + g_{\omega K} \omega_0(\mathbf{r}) + g_{\rho K} R_0(\mathbf{r}) \right] \theta(\mathbf{r}). \end{aligned} \quad (38)$$

The charge density now reads

$$\rho_{\text{ch}}(\mathbf{r}) = \rho_p(\mathbf{r}) - \rho_e(\mathbf{r}) - \rho_K(\mathbf{r}), \quad (39)$$

with the kaon contribution,

$$\rho_K = f_K^2 \theta^2 [\mu_K - V + g_{\omega K} \omega_0(\mathbf{r}) + g_{\rho K} R_0(\mathbf{r})]. \quad (40)$$

Additional parameters concerning kaons are presented in Table 2. By a lattice QCD calculation, the kaon-nucleon sigma term Σ_{KN} is estimated as 290 – 450 MeV [74]. Using the above values and the relation (see Appendix)

$$\frac{g_{\sigma K} g_{\sigma N}}{m_\sigma^2} = \frac{\Sigma_{KN}}{2m_K f_K^2},$$

³We use the meson exchange model (MEM) for kaon Lagrangian to compare our results with the earlier ones [28, 30, 31], which is not chiral-symmetric (see Appendix). Note however that both can well describe the low-energy kaon-nucleon dynamics.

Table 2: Additional parameters used in our RMF model with kaon terms. The kaon optical potential U_K is defined by $U_K = g_{\sigma K}\sigma + g_{\omega K}\omega_0$.

$f_K(\approx f_\pi)$ [MeV]	m_K [MeV]	$g_{\omega K}$	$g_{\rho K}$	$U_K(\rho_0)$ [MeV]
93	494	$g_{\omega N}/3$	$g_{\rho N}$	$-120 - -130$

$g_{\sigma K}$ can be $0.849 - 1.318$. On the other hand, the parameter $g_{\sigma K}$ enters the value of the K^- optical potential U_K defined by $U_K = g_{\sigma K}\sigma + g_{\omega K}\omega_0$. There have been many works trying to extract U_K at the saturation density from the data on the kaonic atoms [75, 76] and from calculations [77, 78, 79, 80, 81], but there is still a controversy about its depth. We take here a somewhat deep potential, as shown in Table 2, to compare our results with the earlier ones [28, 29, 30, 31]. The corresponding $g_{\sigma K}$ can be $2.209 - 2.519$, which may be rather large compared to the lattice QCD estimation. To understand a dependence of the results on the value of U_K we further allow for its variation.

4.2 Properties of kaonic pasta structures

The kaon condensation is considered to be of first order. Therefore it may give rise to non-uniform structures with different geometries, the structured mixed phase. In fact, the system exhibits a series of structure change similar to the nuclear “pasta”: the kaonic droplet, rod, slab, tube, bubble (which we call “kaonic pasta” structures). Figure 13 displays typical density profiles and the Coulomb potential. The neutron distribution proves to be rather flat. The proton distribution on the other hand is strongly correlated with the kaon distribution, which means that the Coulomb interaction is crucial.

In the upper panel of Fig. 14 we depict the energy per nucleon as a function of baryon number density. The dotted line indicates the case of single phase (if one assumes the absence of the mixed phase). In this case uniform matter consists of normal nuclear matter below the critical density and kaonic matter above the critical density. The cross on the dotted line ($\rho_B \simeq 0.46 \text{ fm}^{-3}$) shows the critical density, i.e. the point where kaons begin to condensate in the case of single phase. Pieces of solid curves, on the other hand, indicate energetically favored structures. Droplets begin to appear for $\rho_B > 0.41 \text{ fm}^{-3}$ and smoothly decrease the energy of the system. The mixed phase disappears for $\rho_B > 0.74 \text{ fm}^{-3}$.

The lower panel of Fig. 14 shows the sizes of the lump R and the cell R_W . We find that at the onset density the size of the cell is infinitely large in case of the full calculation. The corresponding steep increase of R_W with decreasing density is clearly seen in the figure. The dashed lines and the dotted line in the lower panel of Fig. 14 show partial contributions to the Debye screening lengths of the electron, proton and kaon, λ_D^e , λ_D^p , and λ_D^K , respectively. We see that in

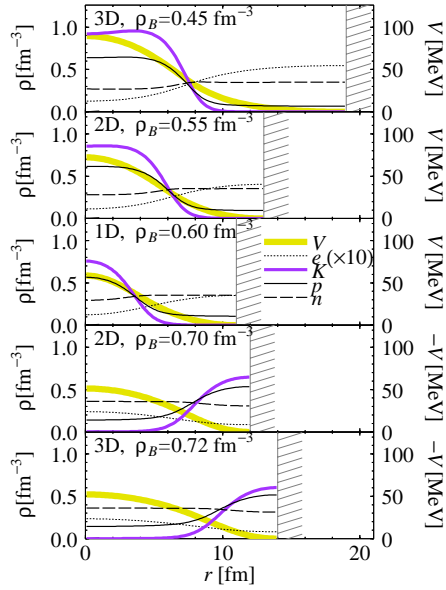


Figure 13: Density profiles of kaonic pasta structures. Here the density does not mean charge-density but number-density of particles. U_K , the kaon optical potential at the nuclear saturation density, is set to be -130 MeV. Displayed using the right axis is the Coulomb potential V .

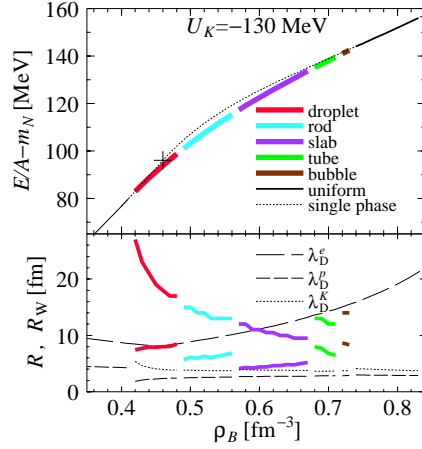


Figure 14: Top: binding energy per nucleon of the nuclear matter in beta equilibrium. The dotted line below the cross shows uniform normal nuclear matter and above the cross, uniform kaonic matter. Bottom: lump size R (thick curves below) and cell size R_W (thick curves above). Compared are the Debye screening lengths of electron, proton and kaon. The Debye screening lengths are calculated using the explicit dependence of μ_a on ρ_a (see Eq. (30)).

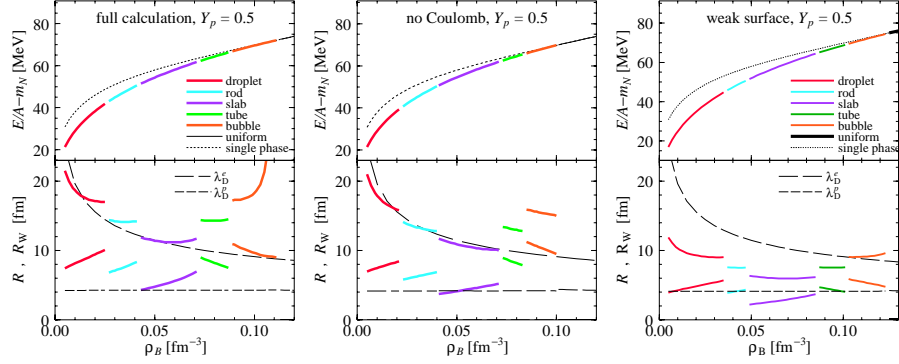


Figure 15: Top: binding energy per nucleon of nuclear matter. Bottom: lump size R and cell size R_W . The proton mixing ratio is $Y_p=0.5$ for all cases. Different calculations are compared. From the left: “full”, “no Coulomb” and “weak surface” calculations. In “no Coulomb” calculation, the electric potential is discarded when determining the density profile and then added to evaluate the energy.

most cases λ_D^e is less than the cell size R_W but is larger than the lump size R . The proton Debye length λ_D^p and the kaon Debye length λ_D^K , on the other hand, are always shorter than R_W and R .

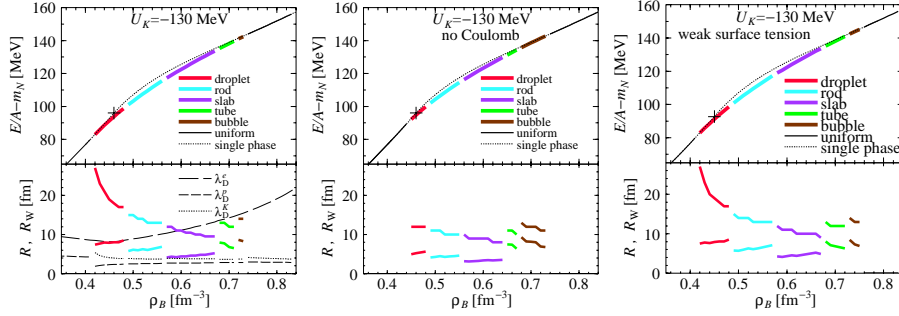


Figure 16: The same as Fig. 15 for high-density nuclear matter in beta equilibrium.

5 Charge screening and surface effects on the pasta structures

5.1 Charge screening effect

To demonstrate the charge screening effects we compare results of the full calculation with those given by a perturbative treatment of the Coulomb interaction often used in the literature, which we refer to as “no Coulomb” calculation. In this calculation the electric potential is discarded in equations of motion (25), (27), (36)–(38), (40) which determine the density profiles. The Coulomb energy is then added to the total energy by using the charge density profile thus determined to find the optimal value with respect to the cell size R_W .⁴

First, we discuss the case of low-density symmetric nuclear matter. In the left and the central panels of Fig. 15, compared are different treatments of the Coulomb interaction. The EOS (upper panels) as a whole shows almost no dependence on the treatments of the Coulomb interaction. However, sizes of the cell and the lump (lower panels), especially for tube and bubbles, are different. In the cases of the “full calculation”, the cell radii of “tube” and “bubble” structures and that of “slab” structure get larger with increase of density, while they are monotonically decreasing in the case of “no Coulomb” calculation. The other effect is a difference in the density range for each pasta structure. The “full” treatment of the Coulomb interaction slightly increases the density region of the nuclear pasta.

We show the same comparison for the kaonic pasta structures in Fig. 16. We see again that the density range of the mixed phase is narrower in the case of the “no Coulomb” calculation than in the full calculation, while the energy gain is almost the same. A remarkable difference is seen in the cell size, especially near the onset density of kaonic pasta, for $\rho_B < 0.5 \text{ fm}^{-3}$. The cell size given by the full calculation is always larger than that given by the “no Coulomb” calculation.

To elucidate the screening effect, we depict the R_W dependence of the energy per nucleon in Fig. 17. In a general case of 3D droplet the Coulomb energy per particle depends on the radius by its square, while the surface energy per particle by its inverse. Therefore the sum of the Coulomb and surface energy has a U-shape (cf. “no Coulomb”) and has a minimum at a certain radius. If the Coulomb interaction is screened, the Coulomb contribution will be suppressed (cf. the full calculation) and the minimum point gets larger (see Fig. 3). Since the cell radius is approximately proportional to the droplet radius for a given baryon density, the above argument applies also to the cell size.

For a long time there existed a naive view that not all the Gibbs conditions can be satisfied in a description by the Maxwell construction if there are two or more independent chemical components [28, 29, 30, 60], because the local charge

⁴This treatment may look similar to the bulk calculation. However, the pressure balance condition is correctly imposed in this calculation, while it is inconsistently used in the bulk calculation.

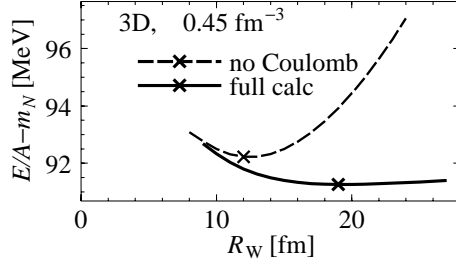


Figure 17: The cell size R_W dependence of the energy per nucleon. Crosses on the curves indicate the minimum points.

neutrality is implicitly assumed in it. As the result of this argument, it was suggested that a broad region of the structured mixed phase may appear in neutron stars. However, in recent papers [61, 62, 65, 63, 64] we have demonstrated that if one properly includes the Coulomb interaction, the Maxwell construction practically satisfies the Gibbs conditions and the range of the mixed phase will be limited.

We present in Fig. 18 the pressure as a function of the baryon-number density. We also depict the pressure when the Gibbs conditions are applied for two semi-infinite matters discarding the Coulomb interaction (indicated by “Gibbs”) and that given by the Maxwell construction (indicated by “Maxwell”). We see that the pieces of solid curves lie between “Gibbs” and “Maxwell”. The full calculation case is more similar to the one given by the Maxwell construction. In Fig. 19 compared are the density profiles obtained by the full and “no Coulomb” calculations. In case of the full calculation the difference between the negative charge density (of kaons and electrons) and the positive charge density of protons is smaller, indicating that the system tends to have a local charge neutrality. These results suggest that the Maxwell construction is effectively justified in the full calculation owing to the charge screening effects.

5.2 Surface effects

If we artificially multiply meson masses m_σ , m_ω and m_ρ by a factor c_M , e.g. $c_M = 1$ (realistic case), 2.5 and 5.0, the surface tension changes. Figure 20 demonstrates the binding energies of finite nuclei calculated with different meson masses. By the use of heavy meson masses, the binding energy of finite nuclei (for finite A) approaches to that of nuclear matter indicated by a thick gray line. This shows that the surface tension is reduced with increase of the meson masses, cf. [82]. Notice that this statement is correct only if we fix the ratio $g_{\phi N}^2/m_\phi^2$.

Using the above modified meson masses, we explore the effects of surface tension in the following. Right panels of Figs. 15 and 16 are EOS and the sizes of the cell and the lump, but now for the case of an artificially suppressed surface tension ($c_M = 5.0$). Comparing them with the left panels, we see that there

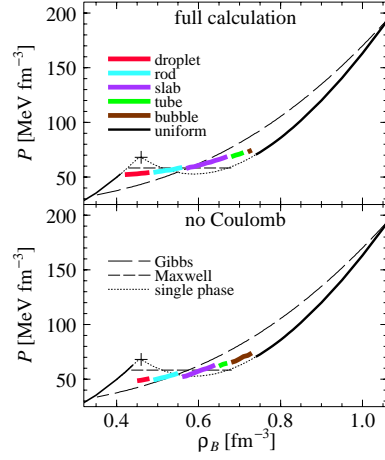


Figure 18: Pressure versus baryon number density.

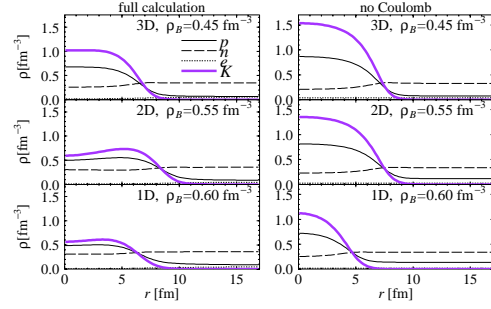


Figure 19: Comparison of density profiles of kaonic matter in full and “no Coulomb” calculations. The cell size, $R_W = 17$ fm, is not optimized since the optimum values would be different for different calculations.

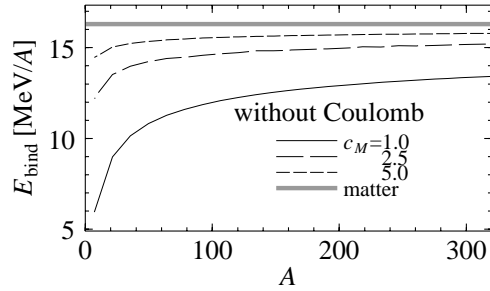


Figure 20: Mass number A dependence of the binding energy of finite nuclei $E_{\text{bind}} = -(E/A - m_N)$ without the Coulomb interaction. Thick gray line shows the case of nuclear matter.

is almost no difference in the EOS. However, there are two differences in the case of low-density nuclear matter. First, the density range of pasta structure is slightly broader for weaker surface tension. Secondly, the cell size with a normal surface tension is larger than the case of weaker one. It means that weaker surface tension and stronger Coulomb repulsion cause the similar effects on the cell size since the pasta structure is realized by the balance of the both.

In the case of kaonic pasta, the meson masses have very small effects. The σ , ω and ρ mesons have less contribution to the surface tension of kaonic pasta but K - N interaction is dominant.

6 Quark pasta structures in the hadron-quark mixed phase

Hereafter, we consider the phase transition from nuclear matter to three-flavor quark matter in beta equilibrium at zero temperature. Accordingly, we must introduce many chemical potentials for the particle species, but the independent ones in this case are reduced to two, the baryon-number chemical potential μ_B and the charge chemical potential μ_Q due to the beta equilibrium and the condition of total charge neutrality. We can easily see that they are equal to the neutron and electron chemical potentials, μ_n and μ_e , respectively. In the mixed phase, these chemical potentials should be spatially constant to satisfy the Gibbs condition (GC), while the density profiles are non-uniform. When we naively apply the Maxwell construction (MC) to get the EOS in thermodynamic equilibrium, we immediately notice that μ_B is constant in the mixed phase, while μ_e is different in each phase because of the difference in the electron number of these phases. This is because the MC uses the EOS of bulk matter in each phase, which is locally charge-neutral, uniform matter; many electrons are needed in hadron matter to compensate for the positive charge of the protons, while in quark matter, total charge neutrality is almost satisfied without electrons. We shall see how this situation is changed in the presence of the Coulomb interaction. Actually we shall see that MC can be effectively used, while it apparently violates the Gibbs conditions.

The treatment of the mixed phase following the deconfinement transition is somewhat different from that in previous sections due to the property of the vacuum. When we consider the mixed phase, hadrons reside in the non-perturbative vacuum, while quarks in the perturbative one. So the change of the vacuum should be also taken into account in this case, which should greatly affect the properties of the interface between the hadron and quark phases. Unfortunately, since dynamics of the deconfinement transition has not been well understood yet, especially in the finite-baryon number density case, we must have recourse to some models. We use the MIT bag-model picture in our study, where the non-perturbative and perturbative vacua are separated by a sharp boundary and the surface is endowed with the surface tension. Note that surface tension is not needed in a consistent calculation, because the non-

uniform density profiles naturally give its effect.

6.1 Thermodynamic potential

We consider the structured mixed phase (SMP) in which one phase is embedded in the other phase with a certain geometrical form. As in the previous studies of low-density nucleon matter and high-density kaonic matter, we use the Wigner-Seitz cell with a size R_W . A cell includes an embedded quark phase with a size R .

The quark phase consists of u , d , and s quarks and electrons. The hadron phase consists of protons, neutrons and electrons. We incorporate the MIT bag model and assume a sharp boundary at the hadron-quark interface. We use the idea of density functional theory (DFT) and incorporate the local density approximation (LDA) [67, 68].

We consider the total thermodynamic potential:

$$\Omega_{\text{total}} = \Omega_H + \Omega_Q + \Omega_\tau, \quad (41)$$

where Ω_H and Ω_Q represent the contributions of the hadron and quark phases, respectively. We here introduce the surface contribution Ω_τ in order to properly treat the geometrical structure. It may be connected with the confining mechanism, but unfortunately we have no definite idea to incorporate it. There have been many estimations about the surface tension in lattice QCD [83, 84], in shell-model calculations [85, 86, 87] and in model calculations based on the dual-Ginzburg Landau theory [88]. Here, we parametrize the surface tension by τ . Then we can write $\Omega_\tau = \tau S$, with S being the area of the interface. Moreover, there may also be a contribution from the curvature term [86], and we regard its effect to be renormalized into τ for simplicity. Actually, many authors have treated the strength of τ as a free parameter and determined how the results depend on its value [55, 57, 58]. Here we also employ this approach by introducing the surface tension parameter τ to simulate the surface effect.

We now present the expressions of thermodynamic potentials. First, the Coulomb interaction energy is expressed in terms of particle densities, as

$$E_V = \frac{1}{2} \sum_{i,j} \int_{V_W} d^3r d^3r' \frac{Q_i \rho_i(\mathbf{r}) Q_j \rho_j(\mathbf{r}')}{|\mathbf{r} - \mathbf{r}'|}, \quad (42)$$

where $i, j = u, d, s, p, n, e$, with Q_i being the particle charge ($Q = -e < 0$ for the electron) and V_W the volume of a Wigner-Seitz cell. Accordingly, the Coulomb potential is defined as

$$V(\mathbf{r}) = - \sum_i \int_{V_W} d^3r' \frac{e Q_i \rho_i(\mathbf{r}')}{|\mathbf{r} - \mathbf{r}'|} + V_0, \quad (43)$$

where V_0 is an arbitrary constant representing the gauge degree of freedom. We here fix the gauge by stipulating the condition $V(R_W) = 0$ as before (see Sec. 2.2).

From the above considerations, we obtain the electron contribution and the Coulomb interaction energy (in both phases) as

$$\begin{aligned}\Omega_{\text{em}} &= \int_{V_{\text{W}}=V_{\text{Q}}+V_{\text{H}}} d^3r \left[-\frac{1}{8\pi e^2} (\nabla V(\mathbf{r}))^2 + \epsilon_e(\rho_e(\mathbf{r})) - \mu_e \rho_e(\mathbf{r}) + V(\mathbf{r}) \rho_e(\mathbf{r}) \right] \\ &= \Omega_{\text{em}}^{\text{Q}} + \Omega_{\text{em}}^{\text{H}},\end{aligned}\quad (44)$$

where $\epsilon_e(\rho_e(\mathbf{r})) = \frac{(3\pi^2 \rho_e(\mathbf{r}))^{\frac{4}{3}}}{4\pi^2}$ is the kinetic energy density of electrons. The contributions in the two phases, $\Omega_{\text{em}}^{\text{Q}}$ and $\Omega_{\text{em}}^{\text{H}}$, are obtained by simply dividing Ω_{em} by the volumes V_{Q} and V_{H} , respectively.

Secondly, in the quark phase, the u and d quarks are treated as massless particles, and only the s quark is massive, with $m_s = 150$ MeV. The kinetic energy density of the quark of flavor f is simply expressed as [89]

$$\epsilon_{f\text{kin}} = \frac{3}{8\pi^2} m_f^4 [x_f \eta_f (2x_f^2 + 1) - \ln(x_f + \eta_f)], \quad (45)$$

where m_f is the quark mass, $x_f = p_{\text{F}f}(\mathbf{r})/m_f$, with the Fermi momentum $p_{\text{F}f}(\mathbf{r}) = (\pi^2 \rho_f(\mathbf{r}))^{\frac{1}{3}}$, and $\eta_f = \sqrt{1 + x_f^2}$.

For the interaction energy, we take into account the leading-order contribution coming from the one-gluon exchange interaction:

$$\epsilon_{f\text{Fock}} = -\frac{\alpha_c}{\pi^3} m_f^4 \left\{ x_f^4 - \frac{3}{2} [x_f \eta_f - \ln(x_f + \eta_f)]^2 \right\}. \quad (46)$$

Including this interaction, the quark contribution to the thermodynamic potential is expressed as

$$\begin{aligned}\Omega_{\text{Q}} &= \Omega_u + \Omega_d + \Omega_s + \int_{V_{\text{Q}}} d^3r B + \Omega_{\text{em}}^{\text{Q}}, \\ \Omega_f &= \int_{V_{\text{Q}}} d^3r [\epsilon_f(\rho_f(\mathbf{r})) - \mu_f \rho_f(\mathbf{r}) - N_f V(\mathbf{r}) \rho_f(\mathbf{r})], \quad N_f = \frac{Q_f}{e},\end{aligned}\quad (47)$$

where the energy density $\epsilon_f(\rho_f(\mathbf{r}))$ represents $\epsilon_{f\text{kin}} + \epsilon_{f\text{Fock}}$ of the f quark, and B is the bag constant. The bag constant is taken as 120 MeV/fm³, and the QCD fine structure constant as $\alpha_c = 0.4$, which were also used by Heiselberg et al. [57] and in Refs. [90, 61, 62].

Thirdly, we consider the hadron contribution. The thermodynamic potential for the non-relativistic nucleons becomes

$$\Omega_{\text{H}} = E_{\text{N}} - \sum_{a=p,n} \mu_a \int_{V_{\text{H}}} d^3r \rho_a(\mathbf{r}) - \int_{V_{\text{H}}} d^3r V(\mathbf{r}) \rho_p(\mathbf{r}) + \Omega_{\text{em}}^{\text{H}}, \quad (49)$$

where E_{N} is the energy of the nucleons,

$$E_{\text{N}} = \int_{V_{\text{H}}} d^3r \left[\sum_{a=p,n} \frac{3}{10m} (3\pi^2)^{\frac{2}{3}} \rho_a^{\frac{5}{3}}(\mathbf{r}) + \epsilon_{\text{pot}}(\rho_p(\mathbf{r}), \rho_n(\mathbf{r})) \right]. \quad (50)$$

Here we use the effective potential $\epsilon_{\text{pot}}(\rho_p(\mathbf{r}), \rho_n(\mathbf{r}))$ parametrized by the local densities for simplicity,

$$\begin{aligned}\epsilon_{\text{pot}}(\mathbf{r}) &= S_0 \frac{(\rho_n(\mathbf{r}) - \rho_p(\mathbf{r}))^2}{\rho_0(\mathbf{r})} + (\rho_n(\mathbf{r}) + \rho_p(\mathbf{r})) \epsilon_{\text{bind}} \\ &+ K_0 \frac{(\rho_n(\mathbf{r}) + \rho_p(\mathbf{r}))}{18} \left(\frac{\rho_n(\mathbf{r}) + \rho_p}{\rho_0} - 1 \right)^2 \\ &+ C_{\text{sat}} (\rho_n(\mathbf{r}) + \rho_p(\mathbf{r})) \left(\frac{\rho_n(\mathbf{r}) + \rho_p(\mathbf{r})}{\rho_0} - 1 \right),\end{aligned}\quad (51)$$

where S_0 , K_0 , ϵ_{bind} and C_{sat} are adjustable parameters which are chosen to reproduce the saturation properties of nuclear matter [90, 61, 62]. We use $S_0 = 18$ MeV, $K_0 = 285$ MeV, and $C_{\text{sat}} = -14.3$ MeV at the saturation density ρ_0 . The value $\epsilon_{\text{bind}} = \tilde{\epsilon}_{\text{bind}} + m_N - 2\rho_0^{-1}\epsilon_p(\rho_B = \rho_0, Y_p = 1/2)$ provides the empirical binding energy $\tilde{\epsilon}_{\text{bind}} = -15.6$ MeV

We consider chemical equilibrium at the hadron-quark interface as well as in each phase, in which case we have the following:

$$\begin{aligned}\mu_u + \mu_e &= \mu_d, \quad \mu_d = \mu_s, \\ \mu_p + \mu_e &= \mu_n \equiv \mu_B, \quad \mu_n = \mu_u + 2\mu_d, \\ \mu_p &= 2\mu_u + \mu_d.\end{aligned}\quad (52)$$

6.2 Numerical procedure

We get the equations of motion from the relation $\frac{\delta \Omega_{\text{total}}}{\delta \phi_i} = 0$ ($\phi_i = \rho_u(\mathbf{r}), \rho_d(\mathbf{r}), \rho_s(\mathbf{r}), \rho_p(\mathbf{r}), \rho_n(\mathbf{r}), \rho_e(\mathbf{r}), V(\mathbf{r})$). The Poisson equation then reads

$$\nabla^2 V(\mathbf{r}) = 4\pi e^2 \rho_{\text{ch}}(\mathbf{r}) \quad (53)$$

where the charge density $\rho_{\text{ch}}^Q(\mathbf{r})$ is given by $\rho_{\text{ch}}(\mathbf{r}) = \frac{2}{3}\rho_u(\mathbf{r}) - \frac{1}{3}\rho_d(\mathbf{r}) - \frac{1}{3}\rho_s - \rho_e(\mathbf{r})$ in the quark phase and $\rho_{\text{ch}}^H(\mathbf{r}) = \rho_p(\mathbf{r}) - \rho_e(\mathbf{r})$ in the hadron phase. The other equations of motion give only the expressions for the chemical potentials,

$$\mu_i = \frac{\delta E_{\text{kin+str}}}{\delta \rho_i(\mathbf{r})} - N_i V(\mathbf{r}), \quad (54)$$

where $E_{\text{kin+str}} = \sum_{i=u,d,s,e} \int d^3r \epsilon_i + E_N$. Then the quark chemical potentials are expressed as

$$\mu_u = \left(1 + \frac{2\alpha_c}{3\pi}\right) \pi^{\frac{2}{3}} \rho_u^{\frac{1}{3}}(\mathbf{r}) - \frac{2}{3} V(\mathbf{r}) \quad (55)$$

$$\mu_d = \left(1 + \frac{2\alpha_c}{3\pi}\right) \pi^{\frac{2}{3}} \rho_d^{\frac{1}{3}}(\mathbf{r}) + \frac{1}{3} V(\mathbf{r}) \quad (56)$$

$$\mu_s = \epsilon_{Fs}(\mathbf{r}) + \frac{2\alpha_c}{3\pi} \left[p_{Fs}(\mathbf{r}) - 3 \frac{m_s^2}{\epsilon_{Fs}(\mathbf{r})} \ln \left(\frac{\epsilon_{Fs}(\mathbf{r}) + p_{Fs}(\mathbf{r})}{m_s} \right) \right] + \frac{1}{3} V(\mathbf{r}), \quad (57)$$

with $\epsilon_{Fs}(\mathbf{r}) = \sqrt{m_s^2 + p_{Fs}^2(\mathbf{r})}$, whereas the chemical potentials of the nucleons and electrons are

$$\begin{aligned}\mu_n &= \frac{p_{Fn}^2}{2m} + \frac{2S_0(\rho_n(\mathbf{r}) - \rho_p(\mathbf{r}))}{\rho_0} + \epsilon_{\text{bind}} \\ &+ \frac{K_0}{6} \left(\frac{\rho_n(\mathbf{r}) + \rho_p(\mathbf{r})}{\rho_0} - 1 \right)^2 + \frac{K_0}{9} \left(\frac{\rho_n(\mathbf{r}) + \rho_p(\mathbf{r})}{\rho_0} - 1 \right) \\ &+ 2C_{\text{sat}} \frac{\rho_n(\mathbf{r}) + \rho_p(\mathbf{r})}{\rho_0} - C_{\text{sat}}\end{aligned}\quad (58)$$

$$\mu_p = \mu_n - \frac{p_{Fn}^2(\mathbf{r})}{2m} + \frac{p_{Fp}^2(\mathbf{r})}{2m} - \frac{4S_0(\rho_B - 2\rho_p(\mathbf{r}))^2}{\rho_0} - V(\mathbf{r}) \quad (59)$$

$$\mu_e = (3\pi^2 \rho_e(\mathbf{r}))^{\frac{1}{3}} + V(\mathbf{r}). \quad (60)$$

We solve these equations of motion under the GC. The important point here is that the Coulomb potential $V(\mathbf{r})$ is included properly in each expression. The Coulomb potential is a function of the charged-particle densities, and, in turn, these densities are functions of the Coulomb potential. As a result, the Poisson equation becomes highly non-linear.

Note that we must now determine eight variables, i.e., six chemical potentials, $\mu_u, \mu_d, \mu_s, \mu_p, \mu_n, \mu_e$, and the radii R and R_W . First, we fix R and R_W . Here we have four conditions due to the beta equilibrium, expressed by (52). Therefore, once the two chemical potentials μ_B and μ_e are given, we can determine the other four chemical potentials, μ_u, μ_d, μ_s and μ_p . Next, we determine μ_e by the global charge neutrality condition:

$$\int_{V_Q} d^3r \rho_{\text{ch}}^Q + \int_{V_H} d^3r \rho_{\text{ch}}^H = 0. \quad (61)$$

The pressure coming from the surface tension ⁵ is given by

$$P_\tau = \tau \frac{dS}{dV_Q}. \quad (62)$$

Then, we find the optimal value of R (R_W is fixed, and therefore f_V changes with R) by using one of the GC,

$$P^Q = P^H + P_\tau. \quad (63)$$

The pressure in each phase, P^Q or P^H , is given by the thermodynamic relation $P^{Q(H)} = -\Omega_{Q(H)}/V_{Q(H)}$, where $\Omega_{Q(H)}$ is the thermodynamic potential in each phase and given by adding an electron and the Coulomb interaction contributions to $\Omega_{Q(H)}$ in Eqs. (47) and (49). Finally, we determine R_W by minimizing

⁵Basically the pressure is locally defined in terms of the Gauss principal curvatures, κ_1 and κ_2 , on the surface: $P_\tau = \tau(\kappa_1 + \kappa_2)$. For the special shapes of sphere, cylinder and plane, R_i is simply constant to give $(\kappa_1, \kappa_2) = (1/R, 1/R)$, $(1/R, 0)$ and $(0, 0)$, respectively.

the thermodynamic potential. Therefore, once μ_B is given, all the other μ_i ($i = u, d, s, p, e$), along with R and R_W , can be obtained.

Note that we keep the GC throughout the numerical procedure. We see below how the mixed phase would be changed by including the finite-size effects, keeping the GC completely. Although the MC is not strictly correct, our results exhibit behavior similar to that in the case of the MC, as a result of including the finite-size effects.

In the numerical calculation, every point inside a cell is represented by a grid point (the number of grid points is $N_{\text{grid}} \approx 100$). The equations of motion are solved by using a relaxation method for a given baryon-number chemical potential under the constraint of global charge neutrality.

7 Charge screening in the hadron-quark mixed phase

7.1 Bulk calculation

First of all we depict the deconfinement transition between uniform hadron matter and quark matter in Fig. 21 by using Eqs. (47), (49) and (51). Then we

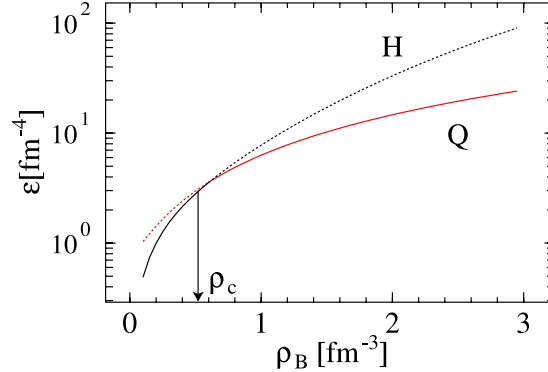


Figure 21: Energy density ϵ for uniform hadron matter and quark matter. Uniform quark matter is energetically favorable in high-density region, while hadron matter in low-density region.

can see that it exhibits the first-order phase transition. To describe the mixed phase a bulk calculation proceeds like this. Considering two semi-infinite matter separated by a sharp boundary and introducing the volume fraction of quark matter f_V , we apply the global charge neutrality condition,

$$f_V \rho_{\text{ch}}^Q + (1 - f_V) \rho_{\text{ch}}^H = 0. \quad (64)$$

Assuming the chemical equilibrium among the particles, there are left two independent quantities to be determined, the electron chemical potential μ_e and

the baryon-number chemical potential $\mu_B = \mu_n$. Finally imposing the pressure balance condition between two phases,

$$P_H = P_Q, \quad (65)$$

we can determine μ_e and f_V for a given μ_B or baryon-number density. We show the EOS in this calculation in Fig. (22). Compared with the EOS given by the

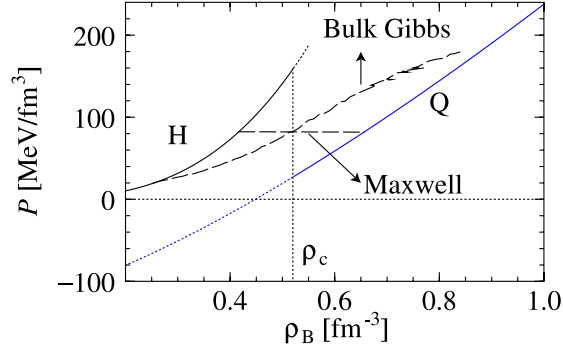


Figure 22: Pressure of uniform matter, that given by the bulk calculation with GC (Bulk Gibbs) and that given by MC (Maxwell).

Maxwell construction, where the local charge neutrality is implicitly assumed instead of Eq. (64), we can see that the density regime of the mixed phase is considerably widened and pressure is no more constant there.

The above picture of the mixed phase is too simple because it should have structures by the surface tension and the Coulomb interaction, which are called the finite-size-effects. Actually Heiselberg et al. demonstrated that the finite-size effects may *energetically* disfavor the mixed phase and thereby its density regime is largely limited [57]. In their calculation, however, the non-uniform structure of the mixed phase is always stable due to an inconsistent inclusion of the Coulomb interaction. We shall see that the rearrangement of the charge density and the charge screening of the Coulomb interaction together may cause a *mechanical* instability of the structured mixed phase. As another defect they use the pressure balance condition before introducing the finite-size effects; they use the value of f_V given by the above simple calculation.

7.2 Mechanical instability

Some analytic discussions have been given in Refs. [61, 62, 90], only by taking the leading contribution of the Coulomb potential in the Poisson equation. We shall see in the next section the numerical results about the properties of the mixed phase and EOS, but it should be useful to figure out some qualitative aspects by analytic discussions. In fact we can clearly see a mechanical instability of the structured mixed phase due to the charge screening effect.

If we expand the charge density in $\delta V(\mathbf{r}) = V(\mathbf{r}) - V_{\text{ref}}$ around the reference value V_{ref} , which is also gauge dependent, the Poisson equation (53) renders

$$\Delta \delta V^\alpha(\mathbf{r}) = 4\pi e^2 \rho^{\text{ch},\alpha}(V^\alpha(\mathbf{r}) = V_{\text{ref}}^\alpha) + (\kappa^\alpha(V^\alpha(\mathbf{r}) = V_{\text{ref}}^\alpha))^2 \delta V^\alpha(\mathbf{r}) + \dots, \quad (66)$$

in each phase $\alpha = Q$ or H with the Debye screening parameter,

$$(\kappa^\alpha(V^\alpha(\mathbf{r}) = V_{\text{ref}}^\alpha))^2 = 4\pi e^2 \left[\frac{\partial \rho^{\text{ch},\alpha}}{\partial V} \right]_{V^\alpha(\mathbf{r})=V_{\text{ref}}^\alpha} = 4 \pi Q_i^\alpha Q_j^\alpha \frac{\partial \rho_j^\alpha}{\partial \mu_i^\alpha} \Big|_{V^\alpha(\mathbf{r})=V_{\text{ref}}^\alpha}, \quad (67)$$

where we used the gauge-invariance relation,

$$\frac{\partial \rho_i^\alpha}{\partial V^\alpha} = N_j^{\text{ch},\alpha} \frac{\partial \rho_j^\alpha}{\partial \mu_i^\alpha}. \quad (68)$$

Then we calculate contribution to the thermodynamic potential (effective energy) of the cell up to $O(\delta V^\alpha(\mathbf{r}))^2$. The Coulomb interaction energy can be written by way of the Poisson equation (66) as

$$E_V = \int_{V_Q} d^3r \epsilon_V^Q + \int_{V_H} d^3r \epsilon_V^H = \int_{V_Q} \frac{(\nabla V^Q(\mathbf{r}))^2}{8\pi e^2} d^3r + \int_{V_H} \frac{(\nabla V^H(\mathbf{r}))^2}{8\pi e^2} d^3r. \quad (69)$$

Besides the terms given by (69), there are another contributions arising from effects associated with the inhomogeneity of the electric potential profile, through implicit dependence of the particle densities on $V^{Q,H}(\mathbf{r})$. We will call them “correlation terms”, $\omega_{\text{cor}}^\alpha = \epsilon_{\text{kin+str}}^\alpha - \mu_i^\alpha \rho_i^\alpha$. Taking $\epsilon_{\text{kin+str}}^\alpha$ and ρ_i^α as functions of $V^\alpha(\mathbf{r})$ we expand them around the reference value V_{ref} to obtain the corresponding correlation contribution to the thermodynamic potential $\Omega_{\text{cor}} = \int_{V_Q} d^3r \omega_{\text{cor}}^Q + \int_{V_H} d^3r \omega_{\text{cor}}^H$:

$$\begin{aligned} \omega_{\text{cor}}^\alpha &= \epsilon_{\text{kin+str}}^\alpha(\rho_i^\alpha(V_{\text{ref}}^\alpha)) - \mu_i^\alpha \rho_i^\alpha(V_{\text{ref}}^\alpha) - \rho^{\text{ch},\alpha}(V_{\text{ref}}^\alpha) V_{\text{ref}}^\alpha \\ &+ \frac{V_{\text{ref}}^\alpha \Delta V^\alpha(\mathbf{r})}{4\pi e^2} + \frac{(\kappa^\alpha(V_{\text{ref}}^\alpha))^2 (\delta V^\alpha(\mathbf{r}))^2}{8\pi e^2} + \dots, \end{aligned} \quad (70)$$

where we also used Eqs. (66) and (67). In general $V_{\text{ref}}^Q \neq V_{\text{ref}}^H$ and they may depend on the droplet size. Their proper choice should provide appropriate convergence of the above expansion in $\delta V(\mathbf{r})$. Taking

$$V_{\text{ref}}^Q = V_{\text{ref}}^H = V_{\text{ref}} = \text{const} \quad (71)$$

we find

$$\omega_{\text{cor}}^\alpha = \frac{(\kappa^\alpha(V_{\text{ref}}))^2 (V^\alpha(\mathbf{r}) - V_{\text{ref}})^2}{8\pi e^2} + \text{const}, \quad (72)$$

and one may count the potential from the corresponding constant value. Here we also took into account that the term $V_{\text{ref}}^\alpha \Delta V^\alpha(\mathbf{r})/(4\pi e^2)$ does not contribute

to Ω according to the boundary conditions in the droplet center, at the droplet boundary (at zero surface charge), and at the boundary of the Wigner-Seitz cell.

The Poisson equation (66) in the droplet phase can be easily solved.⁶ For $r < R$, the charge density $\rho_{\text{ch}}^{\text{Q}}$ can be written as

$$\rho_{\text{ch}}^{\text{Q}} \simeq \left(1 - \frac{2\alpha_c}{\pi}\right) \times \left[\frac{2\mu_B^2(V^{\text{Q}}(\mathbf{r}) - \mu_e)}{9\pi^2} \left(1 + O\left(\frac{(V^{\text{Q}}(\mathbf{r}) - \mu_e)}{\mu_B}\right)\right) + \frac{\mu_B m_s^2}{6\pi^2} \right] \quad (73)$$

by way of Eq. (55) to find

$$V^{\text{Q}}(r) - \mu_e = \frac{V_0^{\text{Q}}}{\kappa^{\text{Q}} r} \sinh(\kappa^{\text{Q}} r) + U_0^{\text{Q}}, \quad (74)$$

with an arbitrary constant V_0^{Q} . For the Debye parameter κ^{Q} and for the constant U_0^{Q} we obtain:

$$(\kappa^{\text{Q}})^2 = \frac{8e^2\mu_B^2}{9\pi} \left(1 - \frac{2\alpha_c}{\pi}\right), \quad U_0^{\text{Q}} \simeq -\frac{3m_s^2}{4\mu_B}. \quad (75)$$

Thus, the value U_0^{Q} is rather small and the main contribution to $V^{\text{Q}}(\mathbf{r})$ comes from the first term in (74). Note that solution (74) is independent of the reference value $V_{\text{ref}}^{\text{Q}}$ in this case, cf. (67), since $\rho_{\text{ch}}^{\text{Q}}$ in (73) is the linear function of $V^{\text{Q}}(\mathbf{r}) - \mu_e$ in the approximation used.

For $r > R$, expanding the charge density $\rho_{\text{ch}}^{\text{H}}(\mathbf{r})$ around a reference value,

$$\rho_{\text{ch}}^{\text{H}}(\mathbf{r}) \simeq \rho_p(V^{\text{H}}(\mathbf{r}) = V_{\text{ref}}^{\text{H}}) + \delta\rho_p(\mathbf{r}) - \rho_e(V^{\text{H}}(\mathbf{r}) = V_{\text{ref}}^{\text{H}}) - \delta\rho_e(\mathbf{r}), \quad (76)$$

we find up to linear order

$$\delta\rho_p(\mathbf{r}) \simeq C_0^{-1}(V^{\text{H}}(\mathbf{r}) - V_{\text{ref}}^{\text{H}}), \quad \delta\rho_e(\mathbf{r}) = \frac{(\mu_e - V_{\text{ref}}^{\text{H}})^2}{\pi^2}(V^{\text{H}}(\mathbf{r}) - V_{\text{ref}}^{\text{H}}), \quad (77)$$

$$C_0 = \frac{A_{22}}{|A|}, \quad p_{\text{Fp}} = (3\pi^2\rho_p(V^{\text{H}}(\mathbf{r}) = V_{\text{ref}}^{\text{H}}))^{1/3},$$

where A_{22} , and $|A|$ are the corresponding matrix element and the determinant of the matrix,

$$A_{ij} = \frac{\delta^2 E_{\text{kin+str}}}{\delta\rho_i \delta\rho_j}. \quad (78)$$

Then the Poisson equation with the boundary condition

$$\nabla V^{\text{H}}(\mathbf{r})|_{r=R_{\text{W}}} = 0 \quad (79)$$

⁶We only consider the quark-droplet phase here for simplicity. See Refs. [61, 62, 90] for other cases.

yields

$$V^H(r) - \mu_e = V_0^H \frac{R}{r} \cosh(\kappa^H(r - R_W)) (1 - \delta) + U_0^H, \quad (80)$$

$$\delta = \tanh(\kappa^H(R_W - r)) / (\kappa^H R_W),$$

with an arbitrary constant V_0^H , where the constant U_0^H is given by

$$U_0^H + \mu_e = -\frac{4\pi e^2 \rho_{\text{ch}}^H (V^H = V_{\text{ref}}^H)}{(\kappa^H)^2} + V_{\text{ref}}^H. \quad (81)$$

The charge screening in the external region is determined by the Debye parameter

$$(\kappa^H)^2 = \frac{4e^2(\mu_e - V_{\text{ref}}^H)^2}{\pi} + \frac{4e^2\pi}{C_0}, \quad (82)$$

where the second term is the contribution of the proton screening. Taking $\rho_B^H = 1.5\rho_0$, $\mu_{e,\text{Gibbs}} \simeq 170$ MeV, $\mu_B = \mu_n \simeq 1020$ MeV, $\alpha_c \simeq 0.4$, we estimate typical Debye screening lengths as $\lambda_D^Q \equiv 1/\kappa^Q \simeq 3.4/m_\pi$, and $\lambda_D^H \equiv 1/\kappa^H \simeq 4.2/m_\pi$, whereas one would have $\lambda_D^H \simeq 8.5/m_\pi$, if the proton contribution to the screening (82) was absent ($C_0^{-1} = 0$). With the estimate $\lambda_D^H \simeq 4.2/m_\pi$ we get that $\kappa^H R_W > 1$ for the droplets with the radii $R > (2f_V)^{1/3} \cdot 3.3/m_\pi$.

In Fig. 23 we demonstrate the radius (R) dependence of the total thermodynamic potential per droplet volume for the case of spherical droplets, $\delta\tilde{\omega}_{\text{tot}}/\beta_0 = (\tilde{\epsilon}_V^Q + \tilde{\epsilon}_V^H + \tilde{\omega}_{\text{cor}}^Q + \tilde{\omega}_{\text{cor}}^H + \tilde{\epsilon}_S)/\beta_0$, given by the sum of partial contributions, where tilde denotes each quantity scaled by the droplet volume $V = 4\pi R^3/3$ and β_0 is a typical quantity with the dimension of the energy density [90, 61, 62],

$$\beta_0 = \frac{3(U_0^H - U_0^Q)^2 (\kappa^Q)^2}{8\pi e^2}. \quad (83)$$

Preparing some wide range for the value of the surface tension parameter τ or $\beta_1 = 3\kappa^Q\tau/\beta_0$ [61, 62, 90], we present two cases of f_V , $f_V = 0.01, 0.5$. The dotted green line shows the asymptotic value of $\delta\tilde{\omega}_{\text{tot}}/\beta_0$ in the limit $\xi \rightarrow \infty$.

The label ‘‘C’’ is given for reference to show the previous non self-consistent case, where the Coulomb potential is not screened (see Fig. 3). We can see that only in the limit of $f_V \ll 1$ and $R \ll \lambda_D^Q$, we are able to recover this case. The ‘‘e.m.’’ curve shows the partial contribution to the thermodynamic potential, $\tilde{\epsilon}_{\text{e.m.}}/\beta_0 \equiv (\tilde{\epsilon}_V + \tilde{\epsilon}_S)/\beta_0$, ignoring correlation terms. Comparing these curves we can see how the screening effect changes the thermodynamic potential: we can see that the minima at the ‘‘e.m.’’ curves disappear already at $\beta_1 > 0.03$, corresponding to unphysically small $\tau \sim$ several MeV/fm². However, the correlation energy gives a sizable contribution to allow the minimum for larger value of τ . Consequently, the minimum totally disappears between $\beta_1 = 0.1$ and $\beta_1 = 0.5$, which may be interpreted as $10 < \tau < 50$ MeV/fm² in this calculation. Thus we have seen a *mechanical instability* of the droplet for the medium values of τ , which might be in the physically meaningful range.

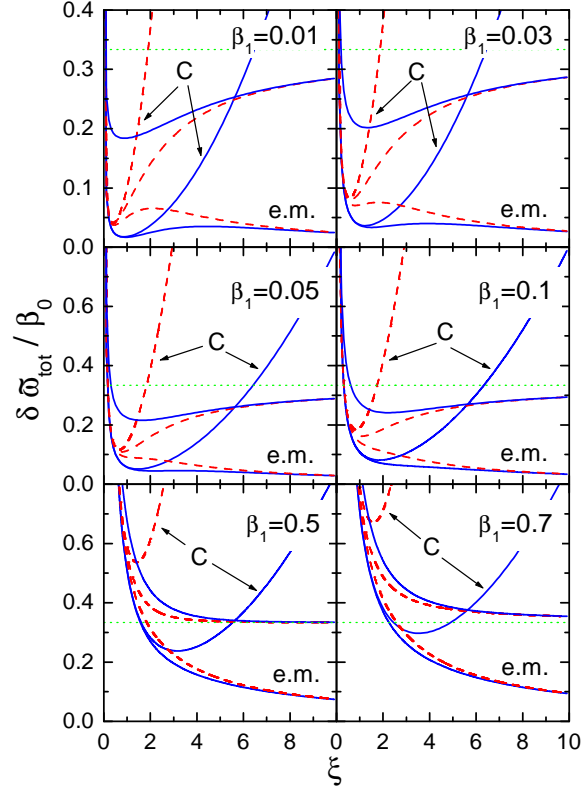


Figure 23: Dimensionless value of the thermodynamic potential per droplet volume. Solid lines are given for $f_V = 0.5$ and dashed lines for $f_V = 1/100$. The ratio of the screening lengths of two phases, $\alpha_0 = \lambda_D^Q / \lambda_D^H$, is fixed as one. ξ is a dimensionless radius of the droplet, $\xi \equiv R / \lambda_D^Q$, with $\lambda_D^Q \simeq 5$ fm in this calculation. See text for further details.

7.3 Charge screening in quark pasta structures

We display the thermodynamic potential in Figs. 24 and 25. In uniform matter, the hadron phase is thermodynamically favorable for $\mu_B < 1225$ MeV, and the quark phase for $\mu_B > 1225$ MeV. Therefore we plot $\delta\omega$, the difference between the thermodynamic potential densities of the mixed phase and each phase of uniform matter:

$$\delta\omega = \begin{cases} \omega_{\text{total}} - \omega_{\text{H}}^{\text{uniform}} & \mu_B < 1225 \text{ MeV}, \\ \omega_{\text{total}} - \omega_{\text{Q}}^{\text{uniform}} & \mu_B \geq 1225 \text{ MeV}. \end{cases} \quad (84)$$

Here, $\omega_{\text{total}} = \Omega_{\text{total}} / V_W$, etc. There we also depict two results for comparison: one is obtained from the bulk calculation, where the finite-size effects are

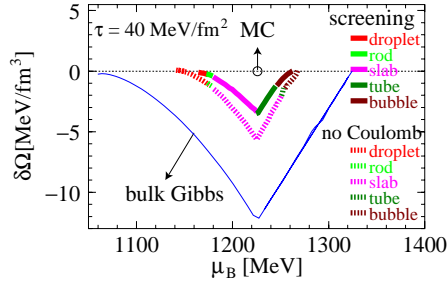


Figure 24: Difference between the thermodynamic potential densities as a function of baryon-number chemical potential μ_B for $\tau = 40$ MeV/fm². If $\delta\omega$ is negative, the mixed phase is the thermodynamically favorable state. The MC determines one point of the phase transition in uniform matter, denoted as a circle in the figure.

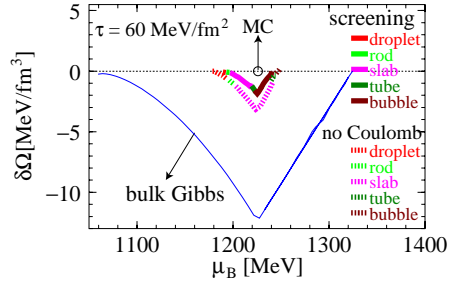


Figure 25: The same as Fig. 24 for $\tau = 60$ MeV/fm². The region of negative $\delta\omega$ is narrower than in the $\tau = 40$ MeV/fm² case.

completely discarded (cf. Fig. 22), and the other is the thermodynamic potential obtained using a perturbative treatment of the Coulomb interaction, which is denoted by “no Coulomb”. We have employed the similar procedure as in Refs. [55, 57, 58]. In this procedure, by discarding the Coulomb potential $V(\mathbf{r})$ to solve the equations of motion Eqs. (55)–(60), each density is determined to be constant in each phase for given R and R_W . Using the chemical equilibrium relation (52) and the charge neutrality condition (61), we can determine its value. The Coulomb interaction energy (42) can be separately evaluated by using the constant densities, and the total thermodynamic potential is obtained by adding it. The remaining procedure is the same as that described in Sec. 6.2: we determine R using the pressure balance relation Eq. (63) and the cell size (R_W) to minimize the total thermodynamic potential.⁷

We can see the screening effects by comparing these “no Coulomb” results with the self-consistent treatment denoted by “screening”. The quantity $\delta\omega$ derived using the MC appears as a point denoted by a circle in Figs. 24 and 25, where only the two conditions $P^Q = P^H$ and $\mu_B^Q = \mu_B^H$ are satisfied. The mixed phase derived with the bulk Gibbs calculation appears over a wide range of values of the μ_B . Therefore, a narrowing the region of the mixed phase signals that the properties of the mixed phase have become closer to those of the MC. It is clearly seen that ω_{total} becomes close to that given by the MC due to the finite-size effects, the effects of the surface tension and the Coulomb interaction. Comparing the result of the self-consistent calculation with that in the case of “no Coulomb”, we can see that the change in energy caused by the screening

⁷Note that they also discarded the size dependence of the particle densities and the surface tension for the pressure balance condition in the bulk calculations [55, 57, 58].

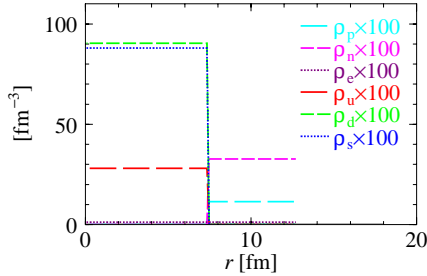


Figure 26: Density profiles in the droplet phase obtained with “no Coulomb” for $\mu_B = 1189$ MeV and $\tau = 60$ MeV/fm². It is seen that they are uniform in each phase. Here, $R = 7.2$ fm and $R_W = 12.8$ fm.

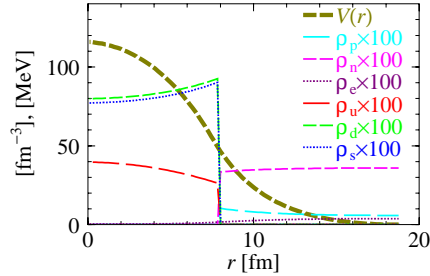


Figure 27: Density profiles and the Coulomb potential derived using the self-consistent calculation for the same parameter set as in Fig. 26. Here $R = 7.7$ fm and $R_W = 18.9$ fm.

effect is not so large, but still the same order of magnitude as that caused by the surface effect. The charge screening effect decreases the Coulomb energy. However, it increases the electron energy instead.

Our parameters are the same as those of Heiselberg et al. [57], and the mixed phase disappears if $\tau > 90$ MeV/fm² in the case of “no Coulomb”. However, in the case of screening, it is rather difficult to estimate the precise value of τ at which the mixed phase disappears, because a mechanical instability would appear for values of τ that are not too large [90, 61, 62]. Nevertheless we could infer that the mixed phase would disappear for $\tau = 70 - 80$ MeV/fm² by referring to the difference between the cases of 40 MeV/fm² (Fig. 24) and 60 MeV/fm² (Fig. 25).

If the surface tension becomes stronger, the relative importance of the screening effect becomes smaller, and the effect of the surface tension becomes more dominant, as seen in Figs. 24 and 25. Although the charge screening does not have so large effect on the bulk properties of matter, we shall see that its effect is significant for the charged particles in the mixed phase, and this brings about a significant change of the properties of the mixed phase.

The charge screening effect induces a rearrangement of the charged particles.⁸ We can see this screening effect by comparing Fig. 26 with Fig. 27. The quark phase is negatively charged, and the hadron phase is positively charged. The negatively charged particles in the quark phase, such as d , s and e , and the positively charged particle in the hadron phase, p , are attracted toward the boundary. In contrast, the positively charged particle in the quark phase, u , and the negatively charged particle in the hadron phase, e , are repelled from the boundary.

⁸In this context, it would be interesting to refer the paper by Heiselberg [91], who studied the screening effect on a quark droplet (strangelet) in the vacuum, and also suggested the importance of the rearrangement of the charged particle densities.

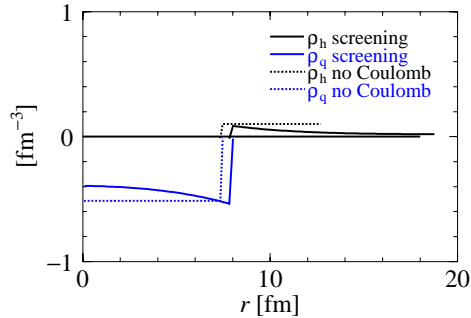


Figure 28: Local charge densities in the case of “no Coulomb” and the case of the self-consistent calculation with the screening effect. For “no Coulomb”, the charge density of each phase is constant over the region. The absolute value of the charge density is larger than that derived from the self-consistent calculation in each phase. In the hadron phase, the charge density almost vanishes near the cell boundary, $r = R_W$.

The charge screening effect also reduces the net charge in each phase. In Fig. 28, we display the local charge densities of the two cases considered in Figs. 26 and 27. The change of the number of charged particles due to the screening is as follows: in the quark phase, the numbers of d and s quarks and electrons decrease, while the number of u quarks increases. In the hadron phase, contrastingly, the number of protons should decrease and the number of electrons should increase. Consequently, the local charge decreases in both phases. In Fig. 28, we can see that the core region of the droplet tends to be charge neutral, and near the boundary of the Wigner-Seitz cell it is almost charge neutral.

In Figs. 29 and 30 we present radii of the lump and cell as functions of density. The R dependence of the total thermodynamic potential comes from the contributions of the surface tension and the Coulomb interaction. The optimal radius representing the minimum of the thermodynamic potential is then determined by the balance between these two contributions. If the Coulomb interaction energy is suppressed, the minimum of the thermodynamic potential is shifted in the direction of larger radius. As a result, the size of the embedded phase R and the cell size R_W become large. In the previous section we have seen that the minimum disappears for a large value of the surface tension parameter, and hence the structure becomes mechanically unstable. We cannot show this directly in our framework, because such unstable solutions are automatically excluded during the numerical procedure, although we can see this tendency in Figs. 29 and 30: R and R_W become larger through the screening effect.

We also see the relation between the size of the geometrical structure and the Debye screening length. The Debye screening length appears in the *linearized*

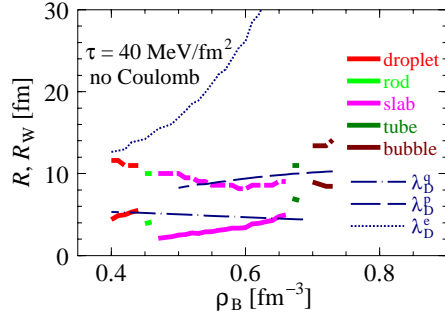


Figure 29: Lump and cell radii derived in the “no Coulomb” calculation. The Debye screening length is also depicted for comparison. R is represented by the thick, solid line and R_W by the thick, dashed line. We can see that the size of the structure becomes less than the Debye screening length.

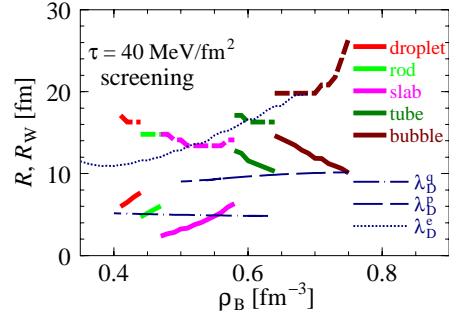


Figure 30: The same quantities as in Fig. 29 derived using the self-consistent calculation with the screening effect. The size of the structure here is larger than that obtained with “no Coulomb”, and exceeds the Debye screening length.

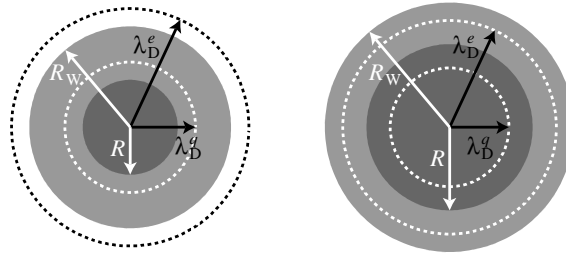


Figure 31: Schematic graphs of the droplet size and the Debye screening length. The right figure corresponds to the case of the self-consistent calculation with the screening effect, and left figure corresponds to the case of “no Coulomb”.

Poisson equation and is given by

$$(\lambda_D^q)^{-2} = 4\pi \sum_f Q_f \left(\frac{\partial \langle \rho_f^{\text{ch}} \rangle}{\partial \mu_f} \right), \quad (\lambda_D^p)^{-2} = 4\pi Q_p \left(\frac{\partial \langle \rho_p^{\text{ch}} \rangle}{\partial \mu_p} \right), \quad (\lambda_D^e)^{-2} = 4\pi Q_e \left(\frac{\partial \langle \rho_e^{\text{ch}} \rangle}{\partial \mu_e} \right), \quad (85)$$

where $\langle \rho_f^{\text{ch}} \rangle$ is the average density in the quark phase, $\langle \rho_p^{\text{ch}} \rangle$ is the average proton number density in the hadron phase, and $\langle \rho_e^{\text{ch}} \rangle$ is the average electron number density inside the cell. The Debye screening length gives a rough measure of the screening effect: at a distance larger than the Debye screening length, the Coulomb interaction is effectively suppressed.

In Fig. 29, we present sizes of the geometrical structure in the case of “no Coulomb”. If we ignore the screening effect, the size of the embedded phase is comparable to or smaller than the corresponding quark Debye screening length, λ_D^q , for a droplet, rod and slab, or the proton Debye screening length, λ_D^p , for a tube and bubble (Fig. 31). This may imply that the Debye screening is not so important. Actually, many authors have ignored the screening effect for the reason elucidated by this argument [57, 58]. In Fig. 30, however, we see that the size of the embedded phase can be larger than λ_D^q (Fig. 31) in the self-consistent calculation. We can also see a similar situation concerning R_W and λ_D^e . This means that the screening has important effects in this mixed phase. We cannot expect such an effect without solving the Poisson equation, because of the non-linearity.⁹

We plot the EOS in Figs. 32 and 33. It is seen that the pressure of the mixed phase becomes similar to that found using the MC. Because a region of local charge neutrality appears due to the screening effect (see Fig. 28), its properties correspond to those derived using the MC.

8 Summary and concluding remarks

We have investigated three forms of non-uniform hadron matter at different density ranges, which correspond to the mixed phases in the first-order phase transitions. As has been discussed by many authors, such non-uniform structures appear as “pasta” structures, i.e. droplet, rod, slab, tube and bubble. By means of mean-field approach under the Wigner-Seitz cell approximation, we have calculated the ground-state density profiles of matter. The size and the dimensionality of the cell were chosen to their optimal values for a given baryon density. Thus we could determine optimal structure of matter along the change of density.

First we have studied the pasta structures in low-density nucleon matter. In this study we have used the relativistic mean-fields (RMFs) as an effective

⁹Within the linear approximation for the charge screening, Iida and Sato have studied the screening effect on quark droplets in a different context [92]. In their case, the electron number density is much larger than in our case, because they considered two-flavor quark matter. Accordingly, the electron screening effect may be dominant, in contrast to the situation in our case.

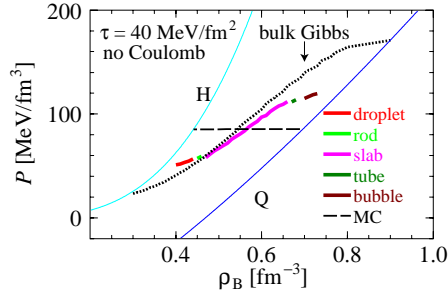


Figure 32: Pressure as a function of the baryon-number density obtained from the “no Coulomb” calculation for $\tau = 40 \text{ MeV/fm}^2$. The results found with the bulk Gibbs calculation and the MC are also presented for comparison.

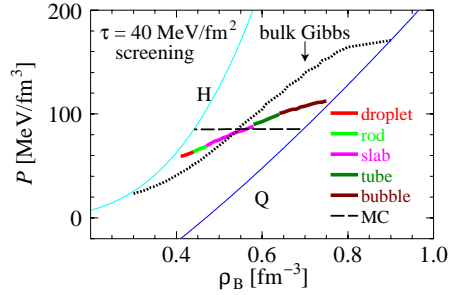


Figure 33: The same quantities as in Fig. 32 computed using the self-consistent calculation with the screening effect.

interaction. The parameter set we have used gives the incompressibility of matter $K = 240 \text{ MeV}$ and the symmetry energy coefficient of 32.5 MeV at the saturation density of symmetric nuclear matter, and can well reproduce the bulk properties of finite systems (nuclei). In nucleon matter with a fixed proton mixing ratio, which corresponds to supernova matter in the collapsing stage, we have observed the nuclear pasta: with increase of density the favorable structure changes from nuclear droplet, rod, slab, tube, and to bubble. Near the saturation density (normal nuclear density), nuclear pasta dissolved to uniform matter. By the appearance of such non-uniform structure, the equation of state of the system becomes significantly soft (the energy gets lower up to 15 MeV/A). In the case of the beta equilibrium (neutron star matter), we did not observe the full pasta structures but only proton droplets appeared in the neutron sea.

Our second target was the kaon condensation at around three times the normal nuclear density, which is relevant to the inner core of neutron stars. Using the same RMF model, we have added the kaonic degree of freedom and could naturally describe both normal nucleon matter and kaonic matter. The surface tension between nucleon matter and kaonic matter is automatically included in the framework. With this model we observed the appearance of pasta structures: kaonic droplet, kaonic rod, etc.

An important advantage of our framework is the consistent treatment of the Coulomb interaction and charged particle distribution: we have included the Coulomb potential in the thermodynamic potential in a gauge-independent way and solved the Poisson equation consistently with the charged particle densities. If we take uniform charge densities as in the bulk calculations, we overestimate the potential energy due to the neglect of the charge screening effect. In fact, we have seen the importance of the charge screening for the properties of the mixed phases; the region of the mixed phase is largely modified, and it may

cause a mechanical instability of the geometrical structure in some cases. As an important consequence of the charge screening effect, the EOS becomes more or less similar to that given by the Maxwell construction which is irrelevant for multiple particle composition. Actually the electron chemical potential should be different in the absence of the Coulomb potential because of the different electron number in two phases. However, we have emphasized that charge chemical potential is only defined after the gauge fixing of the Coulomb potential, so that number densities are not solely given by the chemical potential but by the linear combination of the chemical potential and the Coulomb potential. The different strength of the Coulomb potential in two phases can give the different particle densities, which can resolve an apparent contradiction in the Maxwell construction.

So far, we have explored only nuclear matter in the ground state (zero temperature). However, supernova matter, for example, should be as hot as several MeV. It is naturally expected that the pasta structure will be modified and dissolved at around the critical temperature [71]. Our model is also applicable for not-very-high temperature by modifying the baryon momentum distribution. The structural phase diagram in density-temperature plane should be useful for the discussion of supernova explosion.

We have used the meson exchange model (MEM) to describe the kaon-nucleon interaction. If we use the chiral model instead, it gives a nonlinear Lagrangian including the kaon self-interaction. The thermodynamic inconsistency of the chiral model has been shown within the mean-field approximation [26, 32, 93]: a bulk calculation of the mixed phase consisting of two semi-infinite matter have concluded that we can not construct the mixed phase satisfying the Gibbs conditions. It may be caused by the non-linearity of the kaon field. So, it would be worth studying the chiral model with our framework to see whether the chiral model is really ill defined in a thermodynamic sense.

We have seen that our framework based on RMF can well reproduce the bulk properties of finite nuclei as well as nuclear matter. It should be interesting to describe kaonic nuclei [94, 95, 96, 97] as a direct application of our framework. Then we can get a consistent description of kaonic nuclei by taking into account the Coulomb interaction as well as the K - N interaction [98].

Then our third subject was the mixed phase of hadron-quark phase transition. We have used a rather simple model for this study. Nowadays there have been many studies about the deconfinement transition and its implications on compact stars [3, 4, 55, 56, 57] and relativistic heavy-ion collisions [47, 52, 53, 54]. Let us consider some implications of these results for the structure of hybrid stars. Glendenning and Pei [55] considered some geometrical structures in the mixed phase and conjectured that “crystalline structures” (quark pastas) would appear in the core region of a hybrid star by using the bulk Gibbs calculation. His results predict that the mixed phase should appear for several kilometers. However, we can say that the region of SMP should be narrow in the μ_B space, and the EOS is more similar to that obtained with the MC, due to the finite-size effects.

We have considered the deconfinement transition from non-strange nuclear

matter for simplicity, while realistically we must take into account hyperons. Many people believe that hyperons will mix in nuclear matter at several times of the saturation density [99, 100, 101, 102, 103, 104, 105]. In such a case we must consider the mixed phase by taking into account hyperons as well. One of the interesting consequences may be related to the properties of hybrid stars: actually it has been shown that the admixture of hyperons considerably softens EOS, while the deconfinement transition stiffens EOS again at high-density region [104, 105]. If the stiffening works well, it becomes rather easy to construct hybrid stars. For quark matter we should consider the possibilities of color superconductivity [41, 42] and ferromagnetism [43, 44, 106]. In particular, magnetic properties of quark matter might be related to the strong magnetic field observed in compact stars [107, 108, 109].

Our framework may be applicable for other subjects. One of the interesting subjects may be color superconductivity. There have been many works about color superconductivity, where various first-order phase transitions have been suggested between different types of superconducting phases [110, 111, 112]. Color neutrality as well as charge neutrality should be considered in that case. Accordingly 3rd and 8th gluons should play an important role for global color neutrality.

Acknowledgments

The authors thank M. Alford, M. Baldo, D. Blaschke, A. Bonasera, K. Iida, A. Iwamoto, N. Iwamoto, E. Kolomeitsev, S. Kubis, U. Lombardo, Tomoyuki Maruyama, T. Muto, S. Nishizaki, K. Oyamatsu, C. J. Pethick, S. Reddy, H.-J. Schulze, T. Takatsuka, R. Tamagaki, T. Tanigawa, S. Tsuruta, D. N. Voskresensky, G. Watanabe, F. Weber and M. Yasuhira for their interests and discussions. This work is partially supported by the Grant-in-Aid for the 21st Century COE “Center for the Diversity and Universality in Physics” from the Ministry of Education, Culture, Sports, Science and Technology of Japan. It is also partially supported by the Japanese Grant-in-Aid for Scientific Research Fund of the Ministry of Education, Culture, Sports, Science and Technology (13640282, 16540246).

APPENDIX: Kaon interactions within the chiral model

We have used the meson exchange model (MEM) to describe kaon condensation. When we use the chiral model instead, the thermodynamic potential is given as follows:

$$\begin{aligned}\Omega &= \Omega_B + \Omega_K + \Omega_M + \Omega_e, \\ \Omega_B &= \sum_{a=p,n} \int d^3r \left[\int_0^{k_F,a} \frac{d^3k}{4\pi^3} \sqrt{m_N^{*2} + k^2} - \rho_a \nu_a \right],\end{aligned}$$

$$\begin{aligned}
\Omega_K &= \int d^3r \left[-f^2(\cos\theta - 1) (m_K^{*2} - 2(\mu - V)X_0) - \frac{1}{2}(\mu - V)^2 f^2 \sin^2\theta + \frac{f^2}{2}(\nabla\theta)^2 \right], \\
\Omega_M &= \int d^3r \left[\frac{1}{2}(\nabla\sigma)^2 + \frac{1}{2}m_\sigma^2\sigma^2 + U(\sigma) - \frac{1}{2}(\nabla\omega_0)^2 - \frac{1}{2}m_\omega^2\omega_0^2 - \frac{1}{2}(\nabla R_0)^2 - \frac{1}{2}m_\rho^2 R_0^2 \right], \\
\Omega_e &= \int d^3r \left[-\frac{1}{8\pi e^2}(\nabla V)^2 - \frac{(V - \mu)^4}{12\pi^2} \right], \tag{86}
\end{aligned}$$

where the kaon field is defined as

$$K = \frac{f}{\sqrt{2}}\sin\theta \tag{87}$$

and

$$\begin{aligned}
X_0 &= g_{\omega K}\omega_0 + g_{\rho K}R_0, \\
\mu_p + V &= \nu_p + g_{\omega N}\omega_0 + g_{\rho N}R_0, \\
\mu_n &= \nu_n + g_{\omega N}\omega_0 - g_{\rho N}R_0, \\
m_K^{*2} &= m_K^2 - 2g_{\sigma K}m_K\sigma, \\
m_N^* &= m_N - g_{\sigma N}\sigma. \tag{88}
\end{aligned}$$

Then the equations of motion can be easily written down,

$$\begin{aligned}
-\nabla^2\sigma + m_\sigma^2\sigma &= -\frac{dU}{d\sigma} + g_{\sigma B}(\rho_n^s + \rho_p^s) - 2g_{\sigma K}m_K f^2(\cos\theta - 1), \\
-\nabla^2\omega_0 + m_\omega^2\omega_0 &= g_{\omega N}(\rho_n + \rho_p) + 2f^2 g_{\omega K}(\cos\theta - 1)(\mu - V), \\
-\nabla^2 R_0 + m_\rho^2 R_0 &= g_{\rho N}(\rho_p - \rho_n) + 2f^2 g_{\rho K}(\cos\theta - 1)(\mu - V), \\
\nabla^2 V &= 4\pi e^2 \rho^{ch}, \\
\nabla^2 \theta &= \sin\theta [m_K^{*2} - 2(\mu - V)X_0 - (\mu - V)^2 \cos\theta], \tag{89}
\end{aligned}$$

where

$$\begin{aligned}
\rho^{ch} &= \left[\rho_p - \rho_K - \frac{(\mu - V)^3}{3\pi^2} \right], \\
\rho^K &= (\mu - V)f^2 \sin^2\theta + 2f^2(\cos\theta - 1)X_0.
\end{aligned}$$

We can see how the thermodynamic potential (86) or the equations of motion (89) can recover the previous formulae used in the studies of kaon condensation in uniform matter [26, 32]. The K - N interaction terms are easily extracted from Eq. (89). Discarding V , the kaon source terms for the mean-fields σ, ω, ρ and the nonlinear potential for $\sigma, U(\sigma)$, we have

$$\begin{aligned}
\sigma &= \frac{g_{\sigma N}(\rho_n^s + \rho_p^s)}{m_\sigma^2}, \\
\omega_0 &= \frac{g_{\omega N}(\rho_n + \rho_p)}{m_\omega^2}, \\
R_0 &= \frac{g_{\rho N}(\rho_p - \rho_n)}{m_\rho^2}, \tag{90}
\end{aligned}$$

and

$$\begin{aligned} X_0 &= \frac{g_{\omega N} g_{\omega K}}{m_\omega^2} (\rho_n + \rho_p) + \frac{g_{\rho N} g_{\omega K}}{m_\rho^2} (\rho_p - \rho_n), \\ m_K^{*2} &= m_K^2 - 2m_K \frac{g_{\sigma N} g_{\sigma K}}{m_\sigma^2} (\rho_n^s + \rho_p^s), \end{aligned} \quad (91)$$

for soft kaons. If we impose the following relations among the coupling constants:

$$\begin{aligned} \frac{g_{\sigma N} g_{\sigma K}}{m_\sigma^2} &= \frac{\Sigma_{KN}}{2m_K f^2}, \\ \frac{g_{\omega N} g_{\omega K}}{m_\omega^2} &= \frac{3}{8f^2}, \\ \frac{g_{\rho N} g_{\rho K}}{m_\rho^2} &= \frac{1}{8f^2}, \end{aligned} \quad (92)$$

we can recover the K - N interaction terms dictated by chiral symmetry,

$$\begin{aligned} X_0 &= \frac{1}{4f^2} (\rho_n + 2\rho_p), \\ m_K^{*2} &= m_K^2 - \frac{\Sigma_{KN}}{f^2} (\rho_n^s + \rho_p^s). \end{aligned} \quad (93)$$

Thus we can derive the previous formulae for kaon condensation within the chiral model [26, 32]

To get MEM, we linearize Eqs. (86) and (89) with respect to θ and further add the non-linear terms, $X_0^2 \theta^2$ and $\sigma^2 \theta^2$, in Ω_K .

References

- [1] S. L. Shapiro and S. A. Teukolsky, *Black Holes, White Dwarfs, and Neutron Stars*, (John Wiley & Sons, 1983.)
- [2] T. Muto, T. Takatsuka, R. Tamagaki and T. Tatsumi, Prog. Theor. Phys. Suppl. **112**, 221 (1993).
- [3] N. K. Glendenning, *Compact stars, Nuclear Physics, Particle Physics and General Relativity*, (Springer-Verlag, New York, 2000).
- [4] F. Weber, *Pulsars as Astrophysical Laboratories for Nuclear and Particle Physics*, High Energy Physics, Cosmology and Gravitation Series (IOP Publishing, Bristol, Great Britain, 1999).
- [5] D. G. Ravenhall, C. J. Pethick and J. R. Wilson, Phys. Rev. Lett. **50**, 2066 (1983).
- [6] C. J. Horowitz, M. A. Pérez-García, and J. Piekarewicz, Phys. Rev. **C69**, 045804 (2004).

- [7] S. Tsuruta, Phys. Reports **292** 1 (1998).
- [8] D. G. Yakovlev and C. J. Pethick, Ann. Rev. Astron. Astrophys. **42** 169 (2004).
- [9] D. Page, U. Geppert and F. Weber, *astro-ph/0508056*.
- [10] Y. Mochizuki and T. Izuyama, Astrophys. J. **440**, 263 (1995).
- [11] M. Hashimoto, H. Seki and M. Yamada, Prog. Theor. Phys. **71**, 320 (1984).
- [12] R. D. Williams and S. E. Koonin, Nucl. Phys. **A435**, 844 (1985).
- [13] K. Oyamatsu, Nucl. Phys. **A561**, 431 (1993).
- [14] C. P. Lorenz, D. G. Ravenhall and C. J. Pethick, Phys. Rev. Lett. **70**, 379 (1993).
- [15] K. S. Cheng, C. C. Yao and Z. G. Dai, Phys. Rev. **C55**, 2092 (1997).
- [16] T. Maruyama, K. Niita, K. Oyamatsu, T. Maruyama, S. Chiba, and A. Iwamoto, Phys. Rev. **C57**, 655 (1998).
- [17] T. Kido, T. Maruyama, K. Niita and S. Chiba, Nucl. Phys. **A663-664**, 877 (2000).
- [18] G. Watanabe, K. Iida and K. Sato, Nucl. Phys. **A676**, 445 (2000);
- [19] G. Watanabe, K. Sato, K. Yasuoka and T. Ebisuzaki, Phys. Rev. **C66**, 012801(R) (2002).
- [20] G. Watanabe and K. Iida, Phys. Rev. **C68**, 045801 (2003).
- [21] D. B. Kaplan and A. E. Nelson, Phys. Lett. **B175**, 57 (1986); **B179**, 409(E) (1986).
- [22] G. E. Brown, C. H. Lee, M. Rho and V. Thorsson, Nucl. Phys. **A567**, 937 (1994).
- [23] T. Muto, R. Tamagaki and T. Tatsumi, Prog. Theor. Phys. Suppl. **112**, 159 (1993).
- [24] T. Tatsumi, Prog. Theor. Phys. Suppl. **120**, 111 (1995).
- [25] E. E. Kolomeitsev, D. N. Voskresensky and B. Kämpfer, Nucl. Phys. **A588**, 889 (1995);
E. E. Kolomeitsev and D. N. Voskresensky, Phys. Rev. **C 68**, 015803 (2003).
- [26] J. A. Pons, S. Reddy, P. J. Ellis, M. Prakash and J. M. Lattimer, Phys. Rev. **C62**, 035803 (2000).

- [27] S. Reddy, G. F. Bertsch and M. Prakash, Phys. Lett. **B475**, 1 (2000).
- [28] N. K. Glendenning and J. Schaffner-Bielich, Phys. Rev. **C60**, 025803 (1999).
- [29] M. B. Christiansen and N. K. Glendenning, *astro-ph/0008207*.
- [30] M. Christiansen, N. K. Glendenning and J. Schaffner-Bielich, Phys. Rev. **C62**, 025804 (2000).
- [31] T. Norsen and S. Reddy, Phys. Rev. **C63**, 065804 (2001).
- [32] T. Tatsumi and M. Yasuhira, Nucl. Phys. **A653**, 133 (1999);
M. Yasuhira and T. Tatsumi, Nucl. Phys. **A690**, 769 (2001).
- [33] T. Muto, Prog. Theor. Phys. **89**, 415 (1993);
T. Muto, Nucl. Phys. **A 697**, 225 (2002) ;
T. Muto, *Proc. of VIII International Conference on Hypernuclear and Strange Particle Physics*, Jefferson Lab., 2003, Nucl. Phys. **A**, (2004) to be published.
- [34] C. H. Lee, Phys. Rep. **275**, 197 (1996);
M. Prakash, I. Bombaci, M. Prakash, P. J. Ellis, J. M. Lattimer, R. Knorren, Phys. Rep. **280**, 1 (1997).
- [35] G. E. Brown and H. A. Bethe, Astrophys. J. **423**, 659 (1994).
- [36] G. E. Brown, K. Kubodera, D. Page and P. Pizzecherro, Phys. Rev. **D37**, 2042 (1988).
- [37] T. Tatsumi, Prog. Theor. Phys. **80**, 22 (1988).
- [38] H. Fujii, T. Muto, T. Tatsumi and R. Tamagaki, Nucl. Phys. **A571**, 758 (1994);
H. Fujii, T. Muto, T. Tatsumi and R. Tamagaki, Phys. Rev. **C50**, 3140 (1994).
- [39] D. Page and E. Baron, Astrophys. J. **254**, L17 (1990).
- [40] For reviews, D. H. Rischke, Prog. Part. Nucl. Phys. **52** (2004) 197;
J. Macher and J. Schaffner-Bielich, Eur. J. Phys. **26** (2005) 341 and references therein.
- [41] M. Alford, K. Rajagopal and F. Wilczek, Nucl. Phys. **B64**, 443 (1999);
D. Bailin and A. Love, Phys. Rep. **107** 325 (1984);
As resent reviews, M. Alford, *hep-ph/0102047*;
K. Rajagopal and F. Wilczek, *hep-ph/0011333*
- [42] M. Alford and S. Reddy, Phys. Rev. **D67**, 074024 (2003).
- [43] T. Tatsumi, Phys. Lett. **B489**, 280 (2000).

- [44] T. Tatsumi, T. Maruyama and E. Nakano, Prog. Theor. Phys. Suppl. **153**, 190 (2004).
- [45] E. Nakano, T. Maruyama and T. Tatsumi, Phys. Rev. **D68**, 105001 (2003).
- [46] K. Adcox et al. (PHENIX collaboration), Phys. Rev. Lett. **88**, 022301 (2002);
C. Adler et al. (STAR collaboration), Phys. Rev. Lett. **90**, 082302 (2003).
- [47] For a recent review, B. Müller and J. L. Nagle, *hep-ph/0602029*.
- [48] J. Madsen, Lect. Notes Phys. **516**, 162 (1999).
- [49] K. S. Cheng, Z. G. Dai and T. Lu, Int. Mod. Phys. **D7**, 139 (1998).
- [50] R. D. Pisalski and F. Wilczek, Phys. Rev. Lett. **29**, 338 (1984).
- [51] R. V. Gavai, J. Potvin and S. Sanielevici, Phys. Rev. Lett. **58**, 2519 (1987).
- [52] Y. A. Terasov, Phys. Rev. **C70**, 054904 (2004).
- [53] S. Pratt and S. Pal, Phys. Rev. **C71**, 014905 (2005).
- [54] J. M. Peters and K. L. Haglin, J. Phys. G: Nucl. Part. Phys. **31**, 49 (2005)
- [55] N. K. Glendenning and S. Pei, Phys. Rev. **D52**, 2250 (1995).
- [56] N. K. Glendenning, S. Pei and F. Weber, Phys. Rev. Lett. **79**, 1603 (1997).
- [57] H. Heiselberg, C. J. Pethick and E. F. Staubo, Phys. Rev. Lett. **70**, 1355 (1993).
- [58] M. Alford, K. Rajagopal, S. Reddy, and F. Wilczek, Phys. Rev. **D64**, 074017 (2001).
- [59] E. A. Guggenheim, *Thermodynamics*, (North-Holland, 1977).
- [60] N. K. Glendenning, Phys. Rev. **D46**, 1274 (1992);
N. K. Glendenning, Phys. Rep. **342**, 393 (2001).
- [61] D. N. Voskresensky, M. Yasuhira and T. Tatsumi, Phys. Lett. **B541**, 93 (2002);
T. Tatsumi and D. N. Voskresensky, *nucl-th/0312114*.
- [62] D. N. Voskresensky, M. Yasuhira and T. Tatsumi, Nucl. Phys. **A723**, 291 (2003).
- [63] T. Endo, T. Maruyama, S. Chiba and T. Tatsumi, *nucl-th/0410102*;
T. Endo, T. Maruyama, S. Chiba and T. Tatsumi, *hep-ph/0502216*.
- [64] T. Maruyama, T. Tatsumi, D. N. Voskresensky, T. Tanigawa and S. Chiba, Nucl. Phys. **A749**, 186 (2005).

- [65] T. Tatsumi, T. Maruyama, D. N. Voskresensky, T. Tanigawa and S. Chiba, *nucl-th/0502040*.
- [66] T. Maruyama, T. Tatsumi, D. N. Voskresensky, T. Tanigawa, S. Chiba and T. Maruyama, *nucl-th/0402202*.
- [67] E. K. U. Gross and R. M. Dreizler, *Density functional theory*, Plenum Press (1995).
- [68] R. G. Parr and W. Yang, *Density-Functional Theory of atoms and molecules*, Oxford Univ. Press, 1989.
- [69] T. Maruyama, T. Tatsumi, D. N. Voskresensky, T. Tanigawa and S. Chiba, Phys. Rev. **C72**, 015802 (2005).
- [70] M. Centelles and X. Viñas, Nucl. Phys. **A563**, 173 (1993).
- [71] G. Watanabe, K. Sato, K. Yasuoka and T. Ebisuzaki, Phys. Rev. **C69**, 055805 (2004).
- [72] G. Watanabe, T. Maruyama K. Sato, K. Yasuoka and T. Ebisuzaki, Phys. Rev. Lett. **94**, 031101 (2005).
- [73] T. Muto and T. Tatsumi, Phys. Lett. **B283**, 165 (1992).
- [74] M. Fukugita, Y. Kuramashi, M. Okawa and A. Ukawa, Phys. Rev. **D51**, 5319 (1995).
S.-J. Dong and K.-F. Liu, Nucl. Phys. Pros. Suppl. **B42**, 322 (1995).
- [75] E. Friedman, A. Gal and C. J. Batty, Nucl. Phys. **A579**, 518 (1994);
C. J. Batty, E. Friedman and A. Gal, Phys. Rep. **287**, 385 (1997).
- [76] E. Friedman, A. Gal, J. Mares and A. Cieply, Phys. Rev. **C60**, 024314 (1999).
- [77] T. Waas, N. Kaiser and W. Weise, Phys. Lett. **B365**, 12 (1996);
T. Waas, N. Kaiser and W. Weise, Phys. Lett. **B379**, 34 (1996);
T. Waas and W. Weise, Nucl. Phys. **A625**, 287 (1997).
- [78] A. Ramos and E. Oset, Nucl. Phys. **A671**, 481 (2000).
- [79] J. Schaffner-Bielich, V. Koch and M. Effenberger, Nucl. Phys. **A669**, 153 (2000).
- [80] L. Tolós, A. Ramos and A. Polls, Phys. Rev. **C65**, 054907 (2002).
- [81] J. A. Oller, E. Oset and A. Ramos, Prog. Part. Nucl. Phys. **45**, 157 (2000).
- [82] W. D. Myers and W. J. Swiatecki, Nucl. Phys. **A601**, 141 (1996).
- [83] K. Kajantie, L. Kärkäinen, and K. Rummukainen, Nucl. Phys. **B357**, 693 (1991).

- [84] S. Huang, J. Potvion, C. Rebbi and S. Sanielevici, Phys. Rev. **D43**, 2056 (1991).
- [85] J. Madsen, Phys. Rev. **D46**, 329 (1992).
- [86] J. Madsen, Phys. Rev. Lett. **70**, 391 (1993).
- [87] M. S. Berger and R. L. Jaffe, Phys. Rev. **C35**, 213 (1987).
- [88] H. Monden, H. Ichie, H. Suganuma and H. Toki, Phys. Rev. **C57**, 2564 (1998).
- [89] R. Tamagaki and T. Tatsumi, Prog. Theor. Phys. Suppl. **112**, 277 (1993).
- [90] T. Tatsumi, M. Yasuhira and D. N. Voskresensky, Nucl. Phys. **A718**, 359c (2003).
- [91] H. Heiselberg, Phys. Rev. **D48**, 1418 (1993).
- [92] K. Iida and K. Sato, Phys. Rev. **C58**, 2538 (1998).
- [93] S. Kubis, *astro-ph/0407530*.
- [94] Y. Akaishi and T. Yamazaki, Phys. Rev. **C 65**, 044005 (2002);
T. Yamazaki and Y. Akaishi, Phys. Lett. **B 535**, 70 (2002).
- [95] A. Dote, H. Horiuchi, Y. Akaishi and T. Yamazaki, Phys. Lett. **B 590**, 51 (2004); A. Dote, H. Horiuchi, Y. Akaishi and T. Yamazaki, Phys. Rev. **C 70**, 044313 (2004).
- [96] T. Kishimoto, Phys. Rev. Lett. **83**, 4701 (1999);
M. Iwasaki et al., Nucl. Instrum. Methods Phys. Res. **A 473**, 286 (2001).
- [97] M. Iwasaki et al., *Proc. of VIII International Conference on Hypernuclear and Strange Particle Physics*, Jefferson Lab., 2003, Nucl. Phys. **A**, (2004) to be published;
T. Kishimoto, *ibid.*
T. Suzuki et al., Phys. Lett. **B 597**, 263 (2004);
M. Iwasaki et al., *nucl-ex/0310018*.
- [98] T. Maruyama et al., in progress.
- [99] T. Takatsuka, Prog. Theor. Phys. Suppl. **156**, 84 (2004).
- [100] V. R. Pandharipande, Nucl. Phys. **A178**, 123 (1971).
- [101] M. Baldo, G. F. Burgio and H.-J. Schulze, Phys. Rev. **C61**, 055801 (2000).
- [102] I. Vidana, A. Polls, A. Ramos, L. Engvik and M. Hjorth-Jensen, Phys. Rev. **C62**, 035801 (2001).

- [103] S. Nishizaki, Y. Yamamoto and T. Takatsuka, Prog. Theor. Phys. **105**, 607 (2001);
S. Nishizaki, Y. Yamamoto and T. Takatsuka, Prog. Theor. Phys. **108**, 703 (2002).
- [104] G. F. Burgio, M. Baldo, P. K. Sahu, A. B. Santra, H.-J. Schulze, Phys. Lett. **B526**, 19 (2002);
G. F. Burgio, M. Baldo, P. K. Sahu and H.-J. Schulze, Phys. Rev. **C66**, 025802 (2002).
- [105] C. Maieron, M. Baldo, G. F. Burgio and H.-J. Schulze, Phys. Rev. **D70**, 043010 (2004).
- [106] For a review, T. Tatsumi, E. Nakano and K. Nawa, *hep-ph/0506002*.
- [107] For a review, G. Chanmugam, Annu. Rev. Astron. Astrophys. **30**, 143 (1992).
- [108] P. M. Woods and C. J. Thompson, *astro-ph/0406133*.
- [109] A. I. Ibrahim et al., Astrophys. J. **574**, L51 (2002)
N. Rea et al., Astrophys. J. **586**, L65 (2003).
G. F. Bignami et al., *astro-ph/0306189*.
- [110] F. Neumann, M. Bubballa and M. Oertel, Nucl. Phys. **A714**, 481 (2003).
- [111] I. Shovkovy, M. Hanauske and M. Huang, Phys. Rev. **D67**, 103004 (2003);
for a review, M. Huang, *hep-ph/0409167*.
- [112] S. Reddy and G. Rupak, *nucl-th/0405054*.